Terahertz Waveguide Spectroscopy of Two-Dimensional Plasmons in GaAs

by

C. Thomas Harris

Submitted to the Department of Electrical Engineering and Computer Science
in partial fulfillment of the requirements for the degree of

Master of Science in Computer Science and Engineering

at the

MASSACHUSETTS INSTITUTE OF TECHNOLOGY

September 2010

Author .....
Department of Electrical Engineering and Computer Science
September 3, 2010

Certified by .....
Rajeev J. Ram
Professor of Electrical Engineering
Thesis Supervisor

Accepted by .....
Terry P. Orlando
Chairman, Department Committee on Graduate Students

Terahertz Waveguide Spectroscopy of Two-Dimensional Plasmons in GaAs

by

C. Thomas Harris

Submitted to the Department of Electrical Engineering and Computer Science
on September 3, 2010, in partial fulfillment of the
requirements for the degree of
Master of Science in Computer Science and Engineering

Abstract

The electrical characteristics of high-mobility, two-dimensional electron gas (2DEG) systems, such as GaAs quantum wells, have been well-studied at low frequencies and in extreme conditions of high magnetic fields and ultralow temperatures. While high-frequency excitations of 2DEGs have been examined to some extent from microwave to terahertz (THz) frequencies, a fundamental understanding of the physical properties of 2DEGs in this range have by no means been mastered. To address this matter, this thesis focused on studying a fundamental, high-frequency collective excitation, known as the plasmon, to better understand plasmon damping and coupling mechanisms in GaAs quantum well 2DEGs. The experiments utilized THz waveguide spectroscopy to study the low-temperature behavior of 2D plasmons.

Thesis Supervisor: Rajeev J. Ram
Title: Professor of Electrical Engineering

Acknowledgments

The completion of this thesis would not have been possible without the assistance and guidance of several people. First, I would like to thank Todd Barrick and Emil Kadlec of Sandia National Laboratories (SNL) for helping with carrier lifetime measurements of LT-GaAs and optical fiber coupling of waveguide samples. Denise Webb and John Nogan at the Center for Integrated Nanotechnologies were invaluable in the packaging process of the fiber-coupled coplanar waveguide spectrometer. I am grateful to Eric Shaner for spending time to teach me optics and waveguide-based measurements and for allowing me to use the facilities in his laboratory at SNL. Eric's knowledge of both high-frequency and low-temperature measurements is vast and working with him in the laboratory afforded me a fantastic learning experience. Lastly, I would like to thank Rajeev Ram for participating in this endeavor. Rajeev's breadth of knowledge and expertise in both the electrical and optical characterization of materials was a most appreciated resource, and his cultivation of critical thinking allowed me to better understand numerous aspects of the measurement .

Contents

List of Figures

List of Tables

Chapter 1

Introduction

Low-dimensional solid-state structures such as semiconductor nanowires, carbon nanotubes, single- and bi-layer graphene, and 2-dimensional electron gases (2DEGs) exhibit many physically rich and interesting electronic phenomena, for instance, classical (particle) and quantum (wave) size effects [1], quantized ballistic conductance [2], and the fractional quantum Hall effect [3, 4, 5]. The majority of work conducted towards understanding electronic transport in these systems has been performed predominately using steady-state (DC) methods, where dynamical quantities, such as the mobility scattering time, have been deduced by applying a theoretical model and implementing measured DC transport properties, e.g., electrical resistivity and carrier density. A more direct approach of acquiring dynamical transport properties is through high-frequency and time-resolved measurements. Such measurement methods permit one to probe materials on both time (picosecond to nanosecond) and frequency (0.1 GHz to 1 THz) scales that are relevant to the characteristic rates and energies intrinsic to these systems, allowing one to observe phenomena that may not be apparent from DC measurements alone.

The research presented in this thesis discusses the development of a terahertz (THz) waveguide spectrometer and describes its use in measuring the plasmon resonance of a 2DEG. The spectrometer is comprised of a coplanar waveguide (CPW) and

an ultrafast material known as low-temperature grown gallium arsenide (LT-GaAs). The LT-GaAs, when properly integrated into a CPW, can be fashioned into a THz photoconductive switch, which can be optically excited by means of an ultrafast laser. The waveguide spectrometer implements two THz switches. As one switch generates a sub-picosecond electrical pulse, the CPW both directs the radiation along the guide and couples the radiation (through conductor line and ground plane spacing) into the test sample. A second switch, at a distance along the guide, is used to time-resolve the pulse emerging from the sample. The spectral content of this emerging pulse reveals information regarding the dielectric response function of the test sample.

As a capstone measurement to this work, the plasmon resonance of a GaAs 2DEG heterostructure was measured using the waveguide spectrometer. Terahertz detectors fabricated from GaAs 2DEGs show great promise in their ability to function as dynamically tunable spectrometers (ref.). However, to date, 2DEG THz detectors cannot operate at temperatures above $\approx 100\,\mathrm{K}$ and possess lower-bound noise equivalent powers (NEPs) of $\sim 10^{-8}\,\mathrm{W}/\sqrt{\mathrm{Hz}}$. This measurement of a 2DEG plasmon was conducted to study the damping mechanisms of the plasmon resonance as a function of temperature to provide insight into the dominant plasmon scattering mechanisms over a wide range of temperatures, which has never before been shown. With knowledge of the mechanisms of plasmon resonance damping, one may be able to better engineer a 2DEG THz detector to operate at higher temperatures and with a lower NEP. The following sections elaborate on the premise of waveguide spectroscopy and provide a brief overview on the performance characteristics of contemporary THz detectors and plasmon-based THz detectors.

1.1 Waveguide Spectroscopy

Performing high-frequency measurements on nanoscale or microscale structures requires addressing several technical challenges. The most conventional means of per-

forming high-frequency measurements on small-scale devices is through electrical characterization. However, above $\sim$ 100 GHz, very few commercial, fully-electronic systems suitable for broadband measurements and spectroscopy are available at prices less than $100,000 [6]. And, although many free-space THz sources exist, coupling free-space THz ($\lambda \sim 100\,\mu$m) or GHz ($\lambda \sim 10$ cm) light both into and out of a nano- or microscale structure for transport measurements can be quite challenging, due to the relatively large wavelengths (λ) of radiation required, compared to a micro- or nanostructure's physical size. Efforts in this area of research rely on techniques such a using a lens to focus THz light onto a waveguide, which delivers the radiation to a test specimen through an electrical connection, and measuring the DC response of the nanostructure [7]. Another means of performing high-frequency measurements on micro- and nanostructures is to perform electro-optic (EO) sampling, which utilizes the birefringent nature of a crystal when in the presence of an applied electric field [8]. This technique relies on an optical pump-probe method and permits non-contact characterization of the test specimen. However, the existence of the EO probe head, which contains the birefringent crystal and is placed on close proximity to the specimen, may or may not be a welcome presence, especially for performing low-temperature measurements in a cryostat.

Figure 1-1 shows the electromagnetic spectrum and defines bands of microwave and THz radiation, based on [9]. The microwave region covers a frequency range of 300 MHz to 300 GHz, and the THz region covers 300 GHz to $\sim$ 10 THz frequencies [10]. In the THz radiation band, a transition occurs where contemporary electronics are physically limited and an alternative means, such as optical excitation, must be implemented.

Waveguide spectroscopy overcomes the aforementioned problems encountered in high-frequency measurements by employing ultrafast, semiconductor photoconductive switches to optically generate sub-picosecond voltage pulses "on chip" (comprised of THz frequency content) that can be coupled into the micro- or nanoscale sample

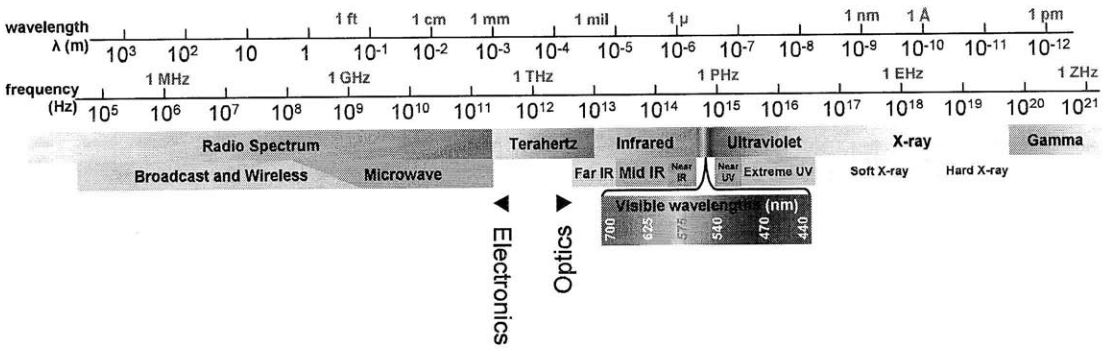

Figure 1-1: The electromagnetic spectrum [9].

of interest through an appropriate waveguide conductor and ground plane arrangement [11, 12]. Furthermore, when adequately designed, optical excitation can be delivered to the device through optical fiber coupling, which is an attractive feature for performing low-temperature measurements in a dilution refrigerator where thermal isolation is critical. A schematic illustration of a coplanar waveguide, equipped with THz photoconductive switches, is given in Fig. 1-2. In this illustration, the waveguide conductor of width w is flanked on both of its sides by ground planes spaced at a distance of s. The conductor and ground planes are often formed from metal (shown in gold in Fig. 1-2) and patterned lithographically on top of an ultrafast material (shown in green in Fig. 1-2).

The break in the CPW conductor line at location L forms what is known as an Auston switch [13]. An Auston switch (described in detail in Chapter 2) is an optoelectronic switch that consists of an ultrafast photoconductive material (LT-GaAs in this work) and two electrodes with a DC voltage bias placed across them. When the LT-GaAs in the region between the two electrodes is optically excited (e.g., by a femtosecond laser), the presence of the electric field results in a charge transfer between the electrodes and produces a voltage transient that possesses a characteristic time determined by the carrier lifetime of the LT-GaAs, τ_r. Auston switches utilizing LT-GaAs can generate voltage pulses as short as $\tau_r \approx 500$ fs or better. As an estimate,

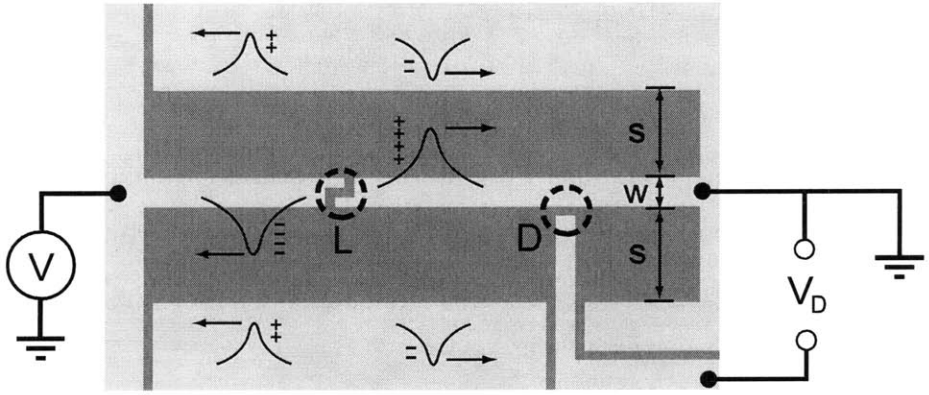

Figure 1-2: A schematic illustration of a general coplanar waveguide (CPW), equipped with THz photoconductive switches for spectroscopy measurements. This top-down view of the CPW shows the waveguide without a specimen mounted on its top surface. L and D represent the launch (pump) and detection (probe) locations along the CPW, respectively. The dashed circles at L and D represent the laser beam spots. Transient positive (+) and negative (-) voltage pulses have been symbolically drawn along the waveguide.

if the voltage pulse is modeled as a transform limited, gaussian pulse, such that the time-bandwidth product $\Delta\omega\Delta t \sim 1$, where $\Delta\omega\,(= 2\pi\Delta f)$ represents the spectral content of the pulse and $\Delta t\,(\approx \tau_r)$ is the temporal extent of the pulse full-width at half-maximum (FWHM), the spectral content of the voltage pulse generated by the Auston switch can be approximated as

$$\Delta f = \frac{1}{2\pi\Delta t} \approx \frac{1}{2\pi\tau_r} \approx 300\,\text{GHz}\ \ \text{(FWHM)}, \tag{1.1}$$

for $\tau_r = 500\,\text{fs}$. Thus, the spectral content of the Fourier-transformed voltage pulse 2 standard deviations away from the pulse center will contain frequencies near 1 THz. Furthermore, employing LT-GaAs of shorter duration τ_r can assist in the achievement of THz frequencies.

By integrating Auston switches into a CPW, one can create a single-shot, THz spectrometer. At the launch point, L, a sub-picosecond electrical pulse is generated by the Auston switch. The accumulated charge on the conductor line couples to the

fundamental transverse electromagnetic (TEM) mode on the on the CPW through charge screening with the adjacent ground planes, which are in close proximity. [1] Due to the switch's symmetry, two, counter propagating electrical pulses of equal spatial extent and opposite charge are "launched" along the conductor [14]. This event is represented by the voltage pulses illustrated in Fig. 1-2, where the pulses have been drawn a few picoseconds after activation of the Auston switch on a conductor line that is $\sim 10\,\text{mm}$ in length. A cross-section of the CPW showing the electric field lines at the location of the rightward traveling pulse (peak value) is displayed in Fig. 1-3 (a). The spacing between the waveguide conductor and the ground plane, s, determines the electric field in the transverse direction of pulse propagation along the CPW. This parameter, s, allows one to tune the electric field such that the propagating pulse may couple appropriately to the characterization sample. Because s is defined lithographically, its value can be $\sim 1\,\mu\text{m}$.

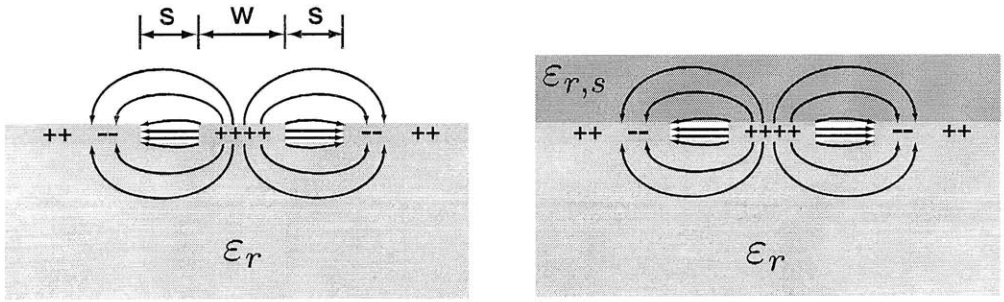

(a) (b)

Figure 1-3: A cross-sectional view of the coplanar waveguide at the location where the rightward traveling pulse peaks in Fig. 1-2. (a) The corresponding field lines between the conductor and the ground planes. The relative permittivity of the substrate is given by ε_r, and the thickness of metallic waveguide is small compared to the thickness of the substrate. (b) The coplanar waveguide with a sample placed on its top surface for characterization. The dielectric response function of the test specimen is $\varepsilon_{r,s}$, which is to be determined.

[1] In the parlance of waveguides, "close proximity" between the waveguide conductor and ground plane is achieved when the spacing s between the conductor and ground plane are a small fraction of the wavelength of interest, i.e., $s \leq \lambda/10$.

As the rightward voltage pulse propagates along the CPW signal line, it ultimately reaches a second Auston switch that is used for sensing this traveling pulse. This switch has been conveniently labeled D for detector. The voltage across D is measured as a probe beam creates free carriers, locally, in the switch gap. In the absence of the voltage pulse, the photogenerated carriers simply recombine. However, when the voltage pulse "sweeps by" D and photogenerated carriers are present, the local electrical field due to the pulse results in free carrier motion and a voltage signal is detected (V_D). This pump-probe method allows one to time-resolve the sub-picosecond voltage pulse traveling along the CPW. Furthermore, multiple detection sites may be employed to examine the dispersion experienced by the pulse as it propagates along the line [11].

To perform high-frequency characterization of a test sample, the specimen is placed on top of the CPW as shown in Fig. 1-3 (b) and is situated between locations L and D, Fig. 1-2. In this arrangement, the propagating voltage pulse interacts with the specimen mounted on top of the CPW. Any spectral content within the voltage pulse that interacts with the mounted specimen will be attenuated, and thus, the voltage pulse sampled at the detection point, D, will be altered, compared to the situation where no sample is present (i.e., free space). If a portion of the spectral content is removed from the voltage pulse (via absorption in the test specimen), an analysis in the frequency domain will reveal notches in the Fourier amplitude, which are indicative of absorption lines. In essence, this spectrometer is similar to the classical experiment where one examines the absorption spectra of a gas in an optically transparent cylinder by shining incident monochromatic light and sweeping frequency and then obtaining an absorption coefficient from the observed attenuation. However, for the waveguide spectrometer, all frequencies of interest are interacting with the specimen simultaneously via the sub-picosecond pulse. Considering the attenuation of spectral intensity in the classical gas spectrometer sense, one can devise a spectral absorption coefficient based on the Beer-Lambert law [15], which may be

written in the following form

$$\alpha(\omega) \approx -\frac{1}{d} \ln \left[\frac{I_D(\omega)}{I_L(\omega)} \right] \tag{1.2}$$

where d is the distance separating the launch and detection points, I_L is the intensity of the launched pulse, I_D is the intensity of the detected pulse, and α is the absorption coefficient. I_L may be determined experimentally by performing a pump-probe measurement solely on the launch site, L. Loss due to modal dispersion in the conductor line can be verified experimentally by time resolving the launched voltage pulse at a location some distance along the CPW, D, in the absence of a test specimen. As will be discussed in Chapter 3, under the quasi-TEM approximation [14] and when the CPW is designed properly, modal dispersion of the picosecond voltage pulse along the CPW can be avoided.

1.2 Terahertz Radiation Detectors

For nearly every region in the electromagnetic spectrum for which a source and detector of a particular frequency of radiation exists, a use has been found for that frequency of light. One interesting region of the electromagnetic spectrum for which many limitations of source and detection schemes exist is at terahertz (THz) frequencies. THz detectors have practical applications in science, such as allowing one to access information regarding the dielectric properties of biological materials or study molecular vibrational and rotational spectra. Because THz-range radiation is non-ionizing (as opposed to x-rays), it could potentially provide a safe means of see-through imaging on humans, e.g., the detection of weapons hidden under clothing, aiding in threat detection.

At ambient temperatures near 300 K, one can fabricate a THz detector from a Shottky diode or by using a Golay cell [16], with each device possessing noise equivalent powers (NEPs) in the range of $10^{-9} - 10^{-10}\,\mathrm{W}/\sqrt{\mathrm{Hz}}$. The silicon bolometer

and superconducting bolometer, both of which require an operating environment of 4 K or less, represent the current sate-of-the-art technology of low-temperature THz detection and exhibit NEPs in the range of $10^{-12} - 10^{-15}\,\mathrm{W}/\sqrt{\mathrm{Hz}}$. The trade-off in implementing the aforementioned low-NEP detection schemes is that they are all broadband detectors, which are not ideal for spectroscopy applications.

In contrast to the aforementioned detection technologies, 2DEG plasmon THz detectors, which possess a carrier-density controlled plasmon resonance, are spectrally tunable, function adequately at higher temperatures (70 - 80 K) than bolometers due to their resonant damping properties, and operate at normal incidence to light, which is useful for constructing focal plane arrays [17]. The drawback of using plasmon THz detectors is that the current NEP to date is $10^{-8}\,\mathrm{W}/\sqrt{\mathrm{Hz}}$.

The most convential means of constructing a plasmon THz detector is to use a two-dimensional electron gas (2DEG). The plasmons in 2DEGs possess very attractive qualities: plasmons have a voltage tunable resonance that enables spectroscopic capabilities in a detector; the resonances rely on free-carriers in otherwise standard semiconductor systems, such as GaAs, SiMOS, and SiGe; and fabrication primarily involves making field effect transistor (FET)-like structures, eliminating any requirements of exotic fabrication. However, very little is known regarding the primary scattering mechanisms of plasmons in a 2DEG. Furthermore, the temperature effects on the performance of 2DEG detectors, which are significant criteria for detector design, are poorly understood.

1.3 Thesis Structure and Organization

The scope of this thesis covers two topics: (1) the design and fabrication of a THz waveguide spectrometer, and (2) low-temperature measurements of plasma oscillations in a 2-dimensional electron gas.

As the first step in developing a THZ waveguide spectrometer was to fabricated

an ultrafast, photoconductive switch, Chapter 2 describes the preparation of LT-GaAs for use as an ultrafast material. To determine the carrier recombination times of various annealed samples of LT-GaAs, optical pump-probe measurements were performed, where the time-resolved reflectivity of the material served as a metric for the material's carrier lifetime. For the spectrometer to sense THz-range frequencies, the LT-GaAs should have a recombination time of $\sim$ 1 ps or less, based on the estimate provided by Eqn. 1.1. To estimate the photoresponse of an Auston switch fashioned from LT-GaAs and integrated into a coplanar waveguide, the dark resistance of such a switch was measured for multiple devices where the LT-GaAs anneal recipe was carefully altered.

Chapter 3 embarks on an experimental study of coplanar waveguides equipped with Auston switches to determine their capabilities as THz waveguide spectrometers. A brief section covering the design of the waveguide is given, along with details of the microfabrication procedure. Free-space pump-probe measurements on coplanar waveguides were performed to obtain a guide topology that provided a suitable time-resolution window for spectroscopy. Implementing an inverted, LT-GaAs/AlGaAs protected, fiber-coupled waveguide, a low-temperature THz waveguide spectrometer was developed. To test the capabilities of this spectrometer, plasmon resonances in a 2DEG were measured at temperatures of 298 K and 10 K.

To conclude the thesis, the major contributions of this work are summarized in Chapter 4 and important directions for future experiments are identified.

Chapter 2

Ultrafast Material Development Using Low-Temperature Grown Gallium Arsenide

2.1 Introduction

Moderately doped, low-defect, single crystal silicon can possess minority carrier lifetimes from 10s of milliseconds to 100s of piceseconds, when heavily doped or defective. For use in ultrafast applications in the late 1970s, D. H. Auston developed a method of ion implanting oxygen into silicon, and thereby creating defect sites to reduce the recombination lifetime to the picosecond range [13]. In the mid 1980s low-temperature grown gallium arsenide (LT-GaAs) emerged and became favored as an ultrafast material due to the fact that it could be epitaxially grown on other III-V layers [18]. Once optimized through proper post-growth annealling conditions, LT-GaAs possesses several attributes that are highly desired in an ultrafast photoconductor: short carrier lifetimes, high carrier mobility [19], and large dark resistivity.

This chapter describes the evolution of LT-GaAs into an ultrafast, photoconductive switch, referred to as an Auston switch [13], and represents the first phase to

fabricating a THz spectrometer. The following sections provide detailed information on the growth and composition of LT-GaAs and a brief explanation of how one fabricates an Auston switch from LT-GaAs.

To optimize the characteristics of an LT-GaAs epitaxial layer for use in an Auston switch, several high-temperature annealing tests were performed. For each annealing test, carrier lifetime measurements were conducted using an all optical pump-probe measurement to correlate the resulting speed of the material with the corresponding anneal. The aim of this work is to increase the dark resistance of an Auston switch as greatly as possible such that the switch exhibits an easily measurable photoresponse, while still retaining ultrafast switching behavior (i.e., short carrier recombination lifetime) for THz generation. The anticipated photoresponse was gauged by integrating an Auston switch into a coplanar waveguide (CPW) and measuring the switches dark resistance. Thereby, allowing one to determine optimal annealing conditions based on the material's carrier lifetime and the switch's dark resistivity.

2.2 LT-GaAs and the Auston Switch

Low-temperature grown GaAs, commonly referred to as LT-GaAs, is an epitaxial layer of GaAs grown at relatively low temperatures (200°C - 300°C) on a semi-insulating GaAs substrate and typically varies in thickness from 0.5μm - 2μm [20, 21, 22]. During the LT-GaAs growth process, excess quantities of As are incorporated into the material. As grown LT-GaAs can exhibit ultrashort photocarrier lifetimes, e.g., $\sim$ 100 fs [22], due to the presence of point defects in the form of As antisites, As interstitials, and Ga-related vacancies. However, in the "as grown" state, the rather large concentration of As precipitates (i.e., clusters) allow for hopping conduction to occur, rendering the material with a low resistivity ($\rho \sim 10\,\Omega$-cm) [20]. With proper care, a post-growth anneal at a temperature near 600°C will thermally liberate a fraction of the As from the volume of the epilayer and remaining As defect sites

will agglomerate to form relatively larger clusters that mitigate hopping conduction, yet permit the material to retain sub-picosecond carrier lifetimes. With appropriate annealing conditions, LT-GaAs can possess both ultrashort photocarrier lifetimes and high resistivity, making LT-GaAs an ideal material for THz photoconductive applications.

By employing an ultrafast material like LT-GaAs, one can fabricate a simple, ultrafast optoelectronic switch, referred to as an Auston switch. An Auston switch, shown in Fig. 2-1, is formed by patterning two metallic conductors on top of an annealed LT-GaAs photoconductive epitaxial layer. For optimal switch performance the LT-GaAs layer should be grown on an insulating GaAs substrate. The LT-GaAs will possess a carrier recombination lifetime of τ_r. Electrons and holes are generated in a region between the two metal conductors by applying an optical pulse of temporal width $< \tau_r$ and photon energy greater than the band gap of the photoconductor. Denoting n and p as the carrier densities of electrons and holes, respectively, a transient carrier distribution will develop due to laser pulsing of the form $n(t) = p(t) \propto I_o e^{-t/\tau_r}$, where t is time and I_o is the incident intensity of the optical pulse. Carriers are collected due to a DC voltage bias applied between the two conductors, during which time a transient voltage signal is produced. The transient voltage signal generated has a first-order decay of the form $V(t) = V_o e^{-t/\tau_r}$, due to carrier recombination, and thus, decay of the photocurrent. The Auston switch is an optoelectronic means of generating sub-picosecond electrical voltage pulses of duration τ_r.

2.3 Carrier lifetime measurements of LT-GaAs

2.3.1 The pump-probe experiment and time-resolved reflectance

In a typical pump-probe measurement, a laser beam consisting of above-band-gap photons is focused to a small spot ($\sim$ 10μm - 1mm) on the surface of the material of interest. Within the volume of absorbed light, a hot electron-hole plasma is generated,

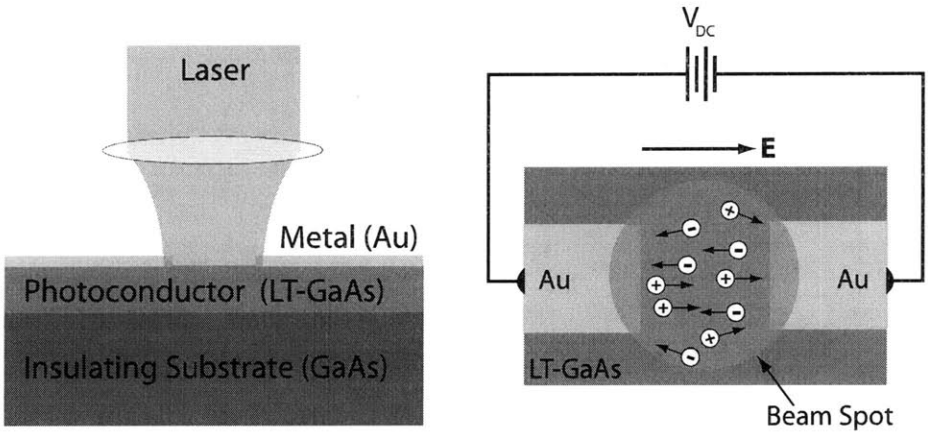

(a) (b)

Figure 2-1: (a) A cross-section of a typical Auston switch, showing the photoconductive LT-GaAs layer that was epitaxially grown on an insulating GaAs substrate with Au metal conductors lithographically patterned on top. Incident photons from a laser beam create photogenerated carriers locally between the two Au leads. (b) A DC voltage bias applied between the two Au leads creates an electric field, sweeping holes to the cathode and electrons to the anode.

which, after a period of time, thermalizes to a quasi-equilibrium distribution through carrier-carrier and carrier-LO (longitudinal-optical) phonon scattering processes [20]. The photoinjected carrier process results in changes to the material's refractive index (Δn). Although the true nature of Δn in this process is related to induced absorption nonlinearities ($\Delta\alpha$), occurring through the mechanisms of bandfilling, band-gap renormalization, and free-carrier absorption [23], here we rely on simple Drude theory of free electrons in a metal or doped semiconductor to gain a qualitative understanding of how a change in carrier density affects a material's reflectivity.

The reflectivity (R) of a metal, semiconductor, or dielectric in free space can be related to the material's index of refraction by means of the Fresnel reflectivity coefficient (r) [15], where, for normal incidence

$$R = |r|^2 = \left|\frac{\tilde{n}-1}{\tilde{n}+1}\right|^2, \tag{2.1}$$

and where $\tilde{n} = n + i\kappa$ is the complex index of refraction. We now recall that the complex index of refraction is related to a material's dielectric function through $\tilde{n} = \sqrt{\varepsilon}$, where

$$\varepsilon(\omega) = 1 + i\frac{\sigma}{\varepsilon_o \omega}. \tag{2.2}$$

Here, σ is referred to as the AC conductivity (ref Ashcroft) and is formulated as

$$\sigma = \frac{\sigma_o}{1 - i\omega\tau} = \frac{Ne^2\tau/m}{1 - i\omega\tau}, \tag{2.3}$$

where ω is the frequency of the light, τ is a average carrier scattering time, m is the mass of a free carrier, and N is the number density of carriers. Often, σ_o is referred to as the DC conductivity. From this simple development, one will note that a change in the carrier density of a material directly affects the material's reflectivity.

A schematic illustration of the pump-probe measurement is shown in Fig. 2-2. This figure presents a time sequence, where an optical pump beam (the stimulus) has generated free carriers in the bulk of the material at a time $t = 0$, Fig. 2-2 (a). Using an optical delay line, a spatially smaller, relatively low power probe beam is made incident upon the region of photogenerated carriers at a time shortly after the pump beam has been terminated, Fig. 2-2 (b). At this instant in time, the probe beam light that is reflected from the material's surface is measured (i.e., the time-resolved response). As time progresses, after the initial stimulation from the pump beam, carriers begin to recombine due to the presence of defects in the material. By delaying the time between the pump and probe beams, one can obtain information about the carrier recombination rate, which is inferred through the change in measured reflectivity from the probe beam, Fig. 2-2 (c).

To determine the carrier lifetime of the annealed LT-GaAs, a standard all-optical pump-probe measurement was employed. For the work performed in this thesis, time-resolved reflectivity data was obtained using a Ti:sapphire, mode-locked laser

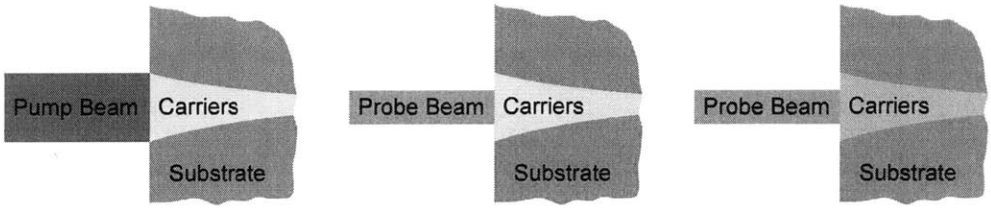

$t = 0$ (a) $t = t_1 << \tau_r$ (b) $t_2 \sim \tau_r$ (c)

Figure 2-2: The optical pump-probe measurement. (a) A laser pump beam creates photogenerated carriers (yellow region) in the optically active substrate, which locally modifies the material's reflectivity. (b) A probe beam that is relatively smaller in both spatial extent (i.e., spot size) and power is made incident on the area where carriers have been generated, with the reflectivity of the probe beam from the surface measured. (c) As the carriers recombine (indicated by the vanishing yellow region), the quantity of reflected probe-beam light reduces. Here τ_r represents the carrier recombination time.

operating at a wavelength near 780 nm. This laser produced pulses of approximately 120 fs widths at a pulse repetition rate of 80 MHz. The pump beam was approximately 100μm in diameter and chopped at 15 kHz, using an acousto-optic modulator (AOM) driven by a lock-in amplifier. Pump and probe beam average power levels were approximately 100-70 mW and 50-30 mW, respectively. A silicon photodiode measured the reflected probe beam power. A photograph of the optical setup and an illustration showing the beam paths is given in Appendix A.

2.3.2 Measurements of carrier lifetime versus annealing temperature

As grown LT-GaAs samples were subjected to a variety of annealing temperatures and annealing times to determine a recipe that would provide one with a photoconductive, ultrafast material. [1] The annealing approach implemented in this work followed an

[1] In this section, focus is placed on correlating the annealing times and temperatures with the carrier lifetime of the LT-GaAs. In the following section, an estimate is provided as to which anneal

ex situ annealing method, where LT-GaAs was grown on a GaAs wafer in a molecular beam epitaxy (MBE) chamber. After the LT-GaAs growth, the wafer was removed from the MBE chamber and exposed to the ambient environment, with an anneal performed as a separate and independent processing step [21]. Another common approach to annealing LT-GaAs relies on *in situ* annealing. In this approach, the wafer is annealed in an As environment, immediately after the LT-GaAs epilayer has been grown [20, 22]. For situations where conserving material is a concern and the proper annealing condition poorly understood, the *ex situ* method allows a wafer to be partitioned into smaller segments and permits various annealing conditions to be explored. The *in situ* approach commits the entire wafer to specific annealing condition. Both *in situ* and *ex situ* methods can provide one with nearly the same quality of ultrafast, highly resistive material. However, *in situ* annealing requires a relatively longer annealing time, with the material possessing a greater sensitivity to the initial wafer growth temperature rather than the annealing temperature [22], and *ex situ* annealing tends to be more sensitive to the post-anneal conditions. Inevitably, both annealing approaches provide the most desirable results at temperatures near 600°C.

All annealing tests were performed in a rapid thermal annealer (RTA) in a reduced argon (i.e., low-pressure) environment. For determining the optimal annealing conditions, three anneal temperatures were chosen: 550°C, 600°C, and 650°C, with a 20 second duration [2] held at the final anneal temperature and a 40 second delay between a brief warm-up temperature of 200°C and the final temperature.

Figure 2-3 shows the results of pump-probe carrier lifetime measurements on the various annealed samples. Time-resolved reflectivity data for the 600°C, 20 s specimen is shown in Fig. 2-3 (a). The initial portion of the peak shown in Fig. 2-3 (a) corresponds to the material accumulating charge in the form of photo-injected car-

recipe results in a suitably responsive, photoconductive switch, as the dark resistances of Auston switches are compared based on various annealing times.

[2] Annealing time durations of 40 s and 60 s were also explored. However, these tests resulted in a much slower material, i.e., $\tau_r \geq 1$ ps.

riers, with the normalized peak corresponding to the time sequence schematically illustrated in Figs. 2-2 (a) and (b). As carriers recombine, the reflectivity signal decays as $\propto e^{-t/\tau_r}$, where τ_r is defined as the carrier recombination time.

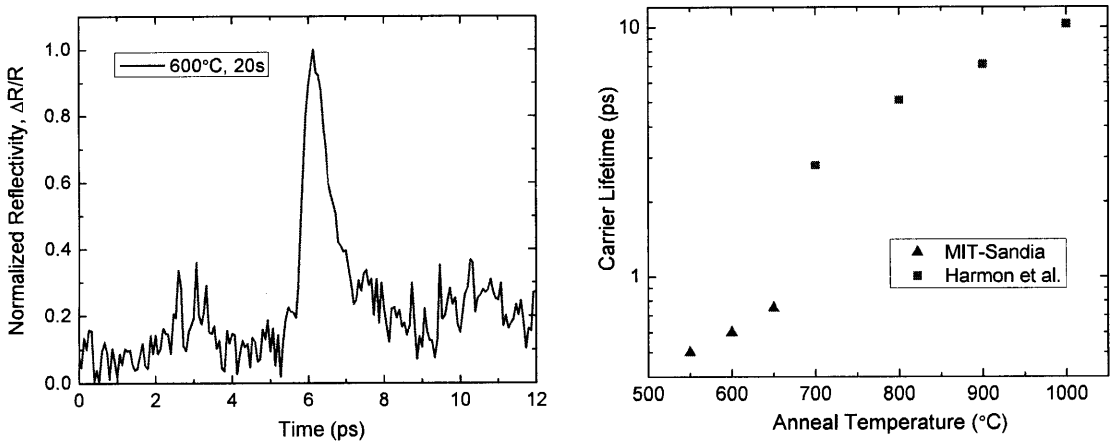

(a) (b)

Figure 2-3: Carrier lifetime measurements of annealed LT-GaAs. (a) Normalized transient reflectivity of LT-GaAs annealed at 600 °C for 20 seconds. The temporal resolution of the measurement is limited by the 120 fs optical pulses from the Ti:Sapphire mode-locked laser. (b) Carrier lifetime data for all samples annealed. For comparison, *ex situ* LT-GaAs annealing data obtained from [21] has been included.

Effective carrier recombination times (τ_r) for the 550°C, 600°C, and 650°C anneals are plotted in Fig. 2-3 (b) and listed in Table 2.1.[3] The carrier lifetimes were obtained by taking the $1/e$ value of the normalized reflectivity plot for each annealing condition. As observed from Table 2.1, the carrier lifetimes become longer as the anneal temperature increases. This effect is due to the reduction of excess As in the epitaxial LT-GaAs layer, and as the temperature increases, more As is liberated from the material [22]. As the excess arsenic content is reduced, τ_r lengthens as the

[3]In the strictest sense, the time-resolved reflectivity is a cross-correlation of the nearly gaussian 120 fs optical laser pulse and the response of the LT-GaAs. Because the known 120 fs laser pulse is approximately an order of magnitude smaller than the measured response, the τ_r reported is taken as $1/e$ of the reflectivity signal and represents an upper-bound to the actual carrier recombination time.

number of defect sites is decimated [22].

Table 2.1: Carrier lifetime of LT-GaAs for various annealing temperatures. The annealing time for each sample was 20 seconds.

Anneal Temperature (°C)	Carrier Lifetime (fs)
Unannealed	200 ± 50
550	500 ± 100
600	600 ± 100
650	750 ± 100

The data obtained by [21] is plotted for comparison in Fig. 2-3 (b). As seen from this plot, the relatively higher anneal temperatures implemented by Harmon (for a duration of 30 s) result in a longer carrier lifetime, with a corresponding increase in lifetime for an increase in temperature.

The impact of growth temperature on the *in situ* annealing process is shown in Fig. 2-4. In this figure the carrier lifetime has been plotted against the LT-GaAs growth temperature for two, disparate annealing temperatures. The carrier lifetimes shown in Fig. 2-4 are comparable to the values listed in Table 2.1, more so than the carrier lifetimes obtained by [21]. A result most likely due to the comparable anneal temperatures implemented by [22] and in this work. An interesting result from the *in situ* anneal performed by [22] show that a relative minima for carrier lifetime as a function of growth temperature exists, with τ_r approaching 100 fs values. However, in the work reported by [22], only values for the carrier lifetime were reported and no claim was made as to the dark resistivity of the material. Thus, although the material they produced was exceptionally fast, it may not be suitable for use in an ultrafast photoconductive switch.

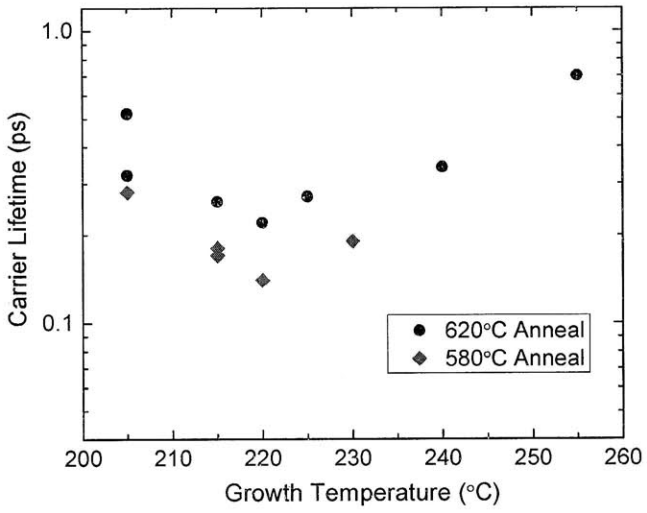

Figure 2-4: Results of *in situ* annealing reported by [22]. The anneal time reported was 10 minutes.

2.4 Evaluation of Auston Switch Dark Resistance

An important physical trait of a high-quality Auston switch is that the switch possesses a relatively large dark resistance (or dark current, for that matter). When functioning, an Auston switch with a large dark resistance will provide an easily detectable photoresponse, compared to a topologically similar switch with a relatively low dark resistance. To ascertain the dark resistance of an Auston switch that was integrated into a coplanar waveguide (CPW), the switch resistance was measured using an HP 34401 digital multimeter in the absence of laboratory light. [4] An optical image of the switch is shown in Fig. 2-5, where a $10\,\mu$m gap exists between a signal line and main conductor line of the CPW, which are the key components of the switch.

[4] A more rigorous evaluation of an Auston switch's photoresponse can be obtained by time resolving an electrical pulse generated by the switch and launched along the waveguide. This measurement is demonstrated in Chapter 3. Here, the dark resistance measurement simply provides a rapid evaluation of the switch's anticipated behavior for various annealing temperatures.

Details of the design and fabrication of the CPW are given in Chapter 3.

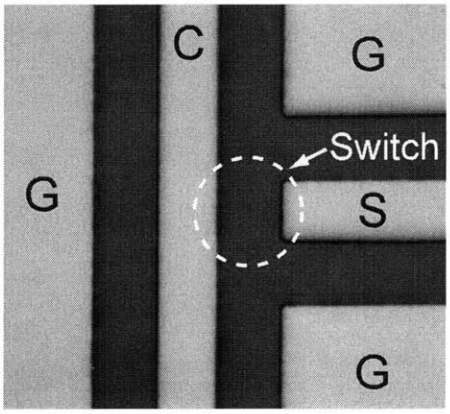

Figure 2-5: An optical image of an Auston switch integrated into a coplanar waveguide, taken at 1000x magnification. The center conductor of the coplanar waveguide is labeled C, with labels G representing the ground planes. Auston switches have been integrated into the waveguide at 2 locations (one location shown here) to both generate and detect THz pulses. The yellow region is gold metal and the gray region is LT-GaAs. The location labeled "switch" approximately defines the region of laser illumination for activating the switch. For scale, the gap between the signal line (S) and the center conductor (C) is $10\,\mu$m.

Measured values of switch dark resistances are listed in Table 2.2. From this table one will observe that the unannealed LT-GaAs sample exhibits the lowest dark resistance, with the sample annealed at 650°C exhibiting the highest dark resistance. This change in dark resistance spans 3 orders of magnitude. As all LT-GaAs samples were annealed for 20 seconds, the effect of the higher temperature anneal is to reduce the quantity of excess As residing in the the epitaxial LT-GaAs layer, which inevitably reduces the effects of hopping conduction in the material and increases its resistivity [22, 24]. An investigation of Auston switches formed with this topology revealed that a lower-bound of acceptable switch resistance was $R_{\text{dark}} \geq 10\,\text{M}\Omega$ [11]. [5] In this study, switches implemented that possessed a dark resistance of $1\,\text{M}\Omega$ or less exhib-

[5]This physical observation was attributed to the intrinsic conductance of the annealed LT-GaAs being greater than the material's conductivity during photoexcitation. Although higher optical powers can be employed, one risks damaging the semiconductor due to heating effects.

ited an almost undetectable photoresponse. Thus, for the LT-GaAs implemented in this work, the anneal temperature of 600°C provides an adequate dark resistance, while retaining a relatively short (< 1 ps) carrier lifetime.

Table 2.2: Measured dark resistances for Auston switches integrated into coplanar waveguides, compare with Fig. 2-5. As excess arsenic is thermally driven from the LT-GaAs epitaxially layer, the dark resistance increases (dark current, for a given voltage, reduces).

Sample	Dark Resistance
Unannealed	324 kΩ
550°C	700 kΩ
600°C	35 MΩ
650°C	> 100 MΩ

2.5 Summary

This portion of the thesis discussed the development of low-temperature grown gallium arsenide (LT-GaAs) for use as an ultrafast photoconductive switch. This type of switch, referred to as an Auston switch, performs optimally when the material of which it is comprised possesses both a short carrier lifetime and a high dark resistance. Low-temperature grown GaAs is naturally endowed with a short carrier lifetime (≈100 fs) due to the excess As content existing in the material. However, the material in the as-grown state can exhibit a relatively low dark resistivity (i.e., large dark current density). To increase the material's dark resistivity, a high temperature anneal is typically performed, which reduces the material's excess As content and mitigates hopping conduction between As precipitates in the LT-GaAs. To optimize the LT-GaAs to function in an Auston switch, a series of annealing tests were performed, with each test followed by a carrier lifetime measurement of the material via optical pump-probe and a measurement of the switch's dark resistance, as observed once integrated into a coplanar waveguide. From the aforementioned tests, an optimal anneal

temperature of 600°C for a duration of 20 seconds was seen to provide both a short carrier lifetime ($\tau_r \approx 600\,\text{fs}$) and a high dark resistance for the switch, $R_{\text{dark}} = 35\,\text{M}\Omega$. Further evidence that these parameters are most suitable for producing ultrafast photoconductive switches in coplanar waveguides is given in the following chapter, where free space pump-probe measurements are implemented to evaluate the performance of the waveguide-switch combination as a THz spectrometer.

Chapter 3

Waveguide Spectroscopy

3.1 Introduction

This chapter describes implementing a coplanar waveguide equipped with Auston switches for use as a spectrometer, utilizing the LT-GaAs material optimization process described in the previous chapter. An Auston switch can be integrated into any location of a waveguide where a break in the main conductor or an electrode in close proximity to the conductor line can be fashioned into the electrodes that comprise the switch. For high-frequency characterization of a material or specimen, which would be performed by placing the sample on top of the waveguide (see Fig. 1-3), architectures such as a microstrip or stripline do not promote a strong coupling to the sample of interest, as the majority of their field lines would exist between the device's conductor line and its ground plane rather than the conductor line and the sample. Coplanar striplines (CPSs) and coplanar waveguides (CPWs) both possess TEM modes that allow sufficient field lines to be present in the sample of interest, such that the test sample can be measured with a reasonable signal-to-noise level. Through both modeling and experimental verification, a picosecond voltage pulse produced from an Auston switch on a CPW exhibits less dispersion during pulse propagation along the waveguide compared to a coplanar strip [11]. For this reason,

coplanar waveguides were chosen for use in the spectrometer developed in this work.

The key components of a CPW are regarded typically to be the guide's effective dielectric constant, ε_{eff}, phase velocity, v_{ph}, and characteristic impedance, Z_o, and are given as

$$\varepsilon_{eff} = \frac{C}{C_o} \tag{3.1}$$

$$v_{ph} = \frac{c}{\sqrt{\varepsilon_{eff}}} \tag{3.2}$$

$$Z_o = \frac{1}{C v_{ph}} \tag{3.3}$$

where c is the speed of light in free space, C is the capacitance of the transmission line, and C_o is the line capacitance in the absence of any dielectric material [25]. To a very good approximation [1], the effective dielectric constant of a CPW may be modeled as

$$\varepsilon_{eff} = \frac{\varepsilon_r + \varepsilon_{r,s}}{2} \tag{3.4}$$

when both the substrate (ε_r) and sample ($\varepsilon_{r,s}$) (compare with Fig. 1-3) are thick compared to the extent of the field lines penetrating the materials [14]. [2] By knowing ε_r, one may obtain the dielectric response function of a test specimen, $\varepsilon_{r,s}$, by measuring v_{ph} with and without the test specimen present on the CPW.

As shown in Fig. 1-3 (a), electric-field lines between the conductor and ground planes of the CPW penetrate the CPW's substrate. Because a picosecond voltage pulse propagating along the CPW is comprised of sinusoids of numerous frequencies,

[1] When the wavelengths that comprise the pulse are large relative to the conductor-groundplane spacing and modal dispersion is not present in the system, i.e., the quasi-TEM limit, this approximation is accurate to within a few percent of a full-wave analysis [25].

[2] This approximation corresponds to one-half of the field lines penetrating the substrate and one-half of the field lines penetrating the sample, which holds for both CPSs and CPWs.

the frequency-dependent nature of the substrate's dielectric constant can result in modal dispersion, where the various frequency components of the pulse propagate along the guide with different phase velocities. To examine the effects of modal dispersion on a standard CPW formed on a GaAs substrate (described in section 3.2.1) and fiber-coupled CPWs that employ a glass substrate (described in section 3.3.1), a closed-form solution developed by [26] for a CPS was implemented as a tool to provide insight. Using the aforementioned model, the effective index of the waveguide for various substrate thicknesses and compositions was computed as a function of frequency and is given in Fig. 3-1. Inspecting the GaAs data, one will note that the effect of thinning the substrate results in mitigating modal dispersion, by increasing the frequency at which the transition from the static effective index to the high-frequency index occurs.

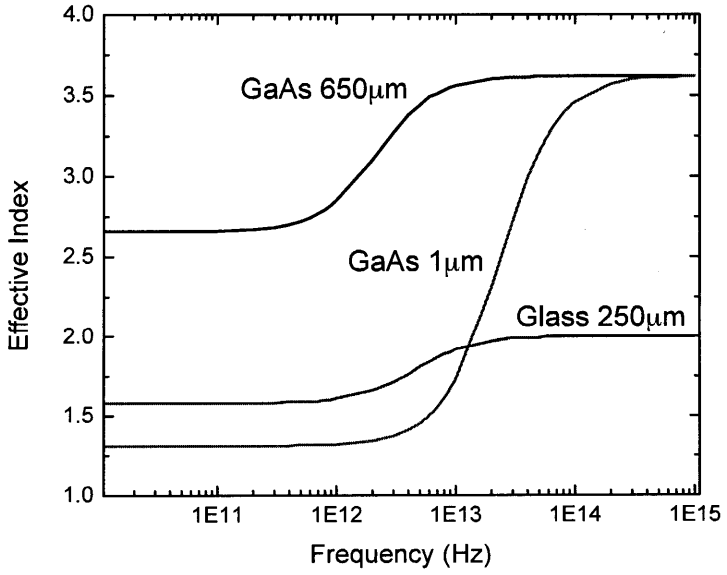

Figure 3-1: The effective index as a function of frequency for a waveguide with both GaAs and glass substrates, based on the model developed by [26] The thicknesses of the GaAs substrates examined were 650 μm and 1 μm, and the thickness of the glass substrate examined was 250 μm. For all of the plots, the conductor width and spacing were both set to 10 μm.

The 650 μm GaAs substrate data shown in Fig. 3-1 exhibits the lowest onset of frequency dependence of the three curves, which approximately occurs beyond 200 GHz. As will be demonstrated in section 3.4.2, the 3 ps voltage pulse achieved in the development of fiber-coupled CPWs possesses a spectral content that extends to approximately 200 GHz. Thus, based on the data presented in Fig. 3-1, one would expect essentially no modal dispersion to be present in the CPW, with the group velocity (v_g) of the voltage pulse being essentially equal to the phase velocity ($v_p h$) of the pulse's constituent frequencies.

Because real conductors do not possess an infinite conductivity, the electric fields on the waveguide penetrate the surface of the conductor by a distance known as the skin depth, $\delta = \sqrt{2/(\omega\sigma\mu_o)}$, where σ is the conductivity of the conductor and μ_o is the permeability of free space. This effect is referred to as intrinsic conductor loss. The surface impedance of the waveguide's conductor lines is given by

$$Z_{\text{surf}} = \frac{1+i}{\sigma\delta} \coth\left[(1+i)\,\frac{t}{\delta}\right], \tag{3.5}$$

with the intrinsic conductor loss formulated as

$$\alpha_{\text{cond}}(\omega) = \mathscr{R}\left[\frac{Z_{\text{surf}}(\omega)}{Z_o}\right] g, \tag{3.6}$$

where $\mathscr{R}$ is the real part of a complex value and g is an additional geometric factor [27].

The following section describes the fabrication and free-space characterization of CPWs with two different probe designs for enabling Auston switches on the conductor line of the waveguide. This measurement was performed to understand how unwanted voltage reflections from the ends of the conductor and probe lines could be mitigated through probe topology adjustments. After a topology was determined, a specialized CPW package was fabricated that allowed fiber coupling to the CPW, such that low-temperature measurements could be performed in a cryostat. Subsequent sections in this chapter discuss the fiber-coupled CPW fabrication and package, the fiber-coupled

optics setup, and the low-temperature measurement of a 2-dimensional electron gas at a temperature of 10 K using the fiber-coupled spectrometer.

3.2 Fabrication and Free-Space Characterization of Coplanar Waveguides

Picosecond voltage pulses generated on and traveling along the CPWs will inevitably encounter a reflective surface, which could be due to the conductor line terminating at the contact pad, a sharp discontinuity in the signal probe line, or the cleaved surfaces of a test specimen placed on top of the CPW. When using the CPW as a spectrometer, such voltage pulses can make data analysis an agonizing process. To avoid pulse reflections due to the test sample, one can almost always make the test sample larger than the CPW, practically speaking. The material discussed in this section is devoted to understanding how one may adjust the CPW pump and probe signal line topology such that unwanted reflections are omitted.

3.2.1 Coplanar Waveguide Fabrication

The CPWs fabricated for free-space characterization were made from an LT-GaAs (0.5 μm) / AlGaAs / GaAs wafer. The wafer was first cleaved into chips of a desired size, with individual pieces of the wafer annealed in a rapid thermal annealer at 600°C for 20 seconds to optimize the behavior of the LT-GaAs for use in an Auston switch, as described in Chapter 2. After the annealing process, individual cleaved pieces were cleaned using an acetone and isopropyl alcohol rinse. Waveguide patterns were made by spinning AZ5214E photoresist onto each chip and softbaking at 90°C for 90 seconds. Using contact lithography with an MJB3 mask aligner the resist was exposed to a dose of 20 mJ/cm^2 of 400 nm light for 4.2 seconds. After development in MIF 300 developer for 30 seconds, the chips were rinsed with a 20:1 deionized

water/ammonium hydroxide solution for 10 seconds and placed immediately in an electron beam evaporator. After an adequate pressure was reached (P$\sim 10^{-7}$ Torr) a Ti/Au layer was evaporated onto each patterned chip and a standard liftoff procedure was performed using acetone. The resulting device is shown in Fig. 3-2.

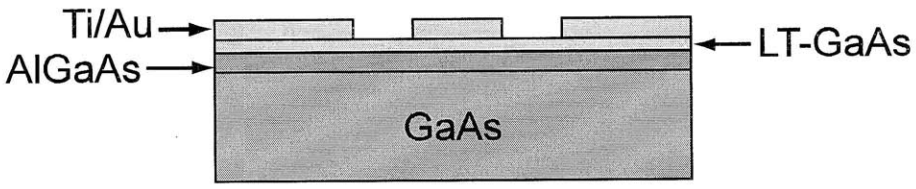

Figure 3-2: Device fabrication of the CPW implemented for free-space testing. The cross-section of the CPW shown here is a more detailed version of that given by Fig. 1-3. The stack consists of 20nm/250nm of Ti/Au, 0.5 μm of LT-GaAs, and 0.5 μm of $Al_{0.55}GaAs_{0.45}$ on a 650 μm GaAs substrate.

3.2.2 Free-space CPW Characterization

Implementing the optical setup used previously for carrier lifetime measurements of LT-GaAs (Chapter 2), pump and probe measurements were performed at room temperature on CPWs by separating the pump and probe laser beams by approximately 2 mm to optically excite the Auston switches at the launch (L) and detection (D) points. A CPW test sample mounted in the optical setup for characterization is given in Fig. 3-3.

The voltage for the launch site was produced by a Keithley 2400 source-measurement unit and the probe voltage at the detection site (V_D, see Fig. 1-2) was measured using a Signal Recovery 7265 lock-in amplifier, which drove the AOM that optically chopped the pump beam. Two CPW pump and probe signal line topologies were chosen for this experiment and are both given in Fig. 3-4. The topology illustrated in Fig. 3-4 (a) was chosen to revisit the work performed in [11], with the topology chosen in Fig. 3-4 (b) used as a comparison to determine if unwanted reflections due to the

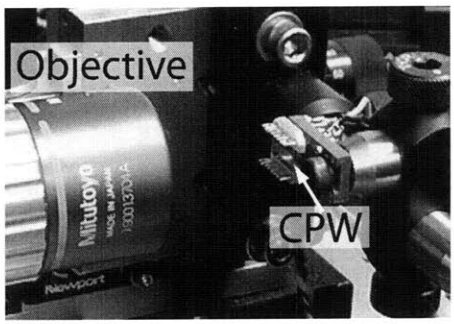

Figure 3-3: CPW mounted to a 16-pin DIP header with Au wire bonds for DC biasing the center conductor at the launch point and for voltage sensing at the waveguide detection site.

angular pump and probe signal lines shown in Fig. 3-4 (a) could be reduced. As a first attempt in topology design, the bend radius shown in Fig. 3-4 (b) was chosen to be 1 mm. Because the LT-GaAs material was inexpensive and the CPW fabrication relatively simple, measurement and iteration of the bend radius through experiments was chosen as the most expeditious route to understanding the effects of arcing the signal line, rather than through modeling and simulation.

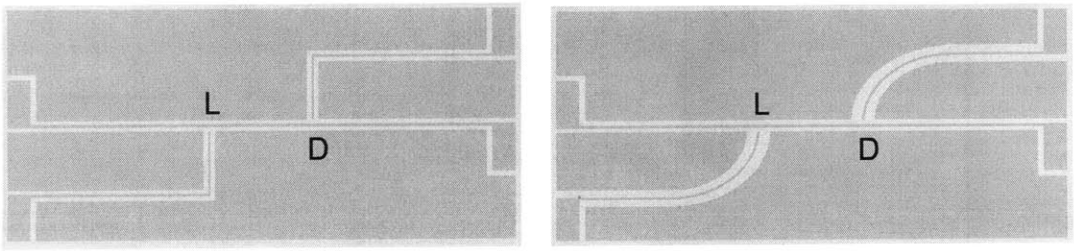

(a) (b)

Figure 3-4: Coplanar waveguide pump and probe signal line topologies, denoted by L and D, respectively. (a) A rectangular topology for the Auston switch pump and probe signal lines and (b) a softer, curved topology. The rectangular regions on the right- and left-hand sides of both CPWs represent wire-bond pads, with the gold color representing a Ti/Au metal layer and the light green color representing the LT-GaAs layer.

Pump and probe measurement results for the CPW topologies shown in Fig. 3-4 are presented in Fig. 3-5. In this plot of data, the voltage pulse was shifted to be

centered at $t = 0$ seconds. An improvement in topologies is immediately obvious as the rectangular signal design shows unwanted reflections at a time of 20 picoseconds following the initial pulse, whereas the curved design extends to approximately 70 picoseconds after the initial pulse is sampled at the detector site D. [3] The significance of this result lies in the additional viable spectral content of the curved CPW design. Without the presence of unwanted voltage reflections, observing the effects of a test sample measured with the waveguide becomes a more tractable process. The importance of this effect will be appreciated more in section 3.4, when measurements of a 2DEG's plasmon resonance are performed.

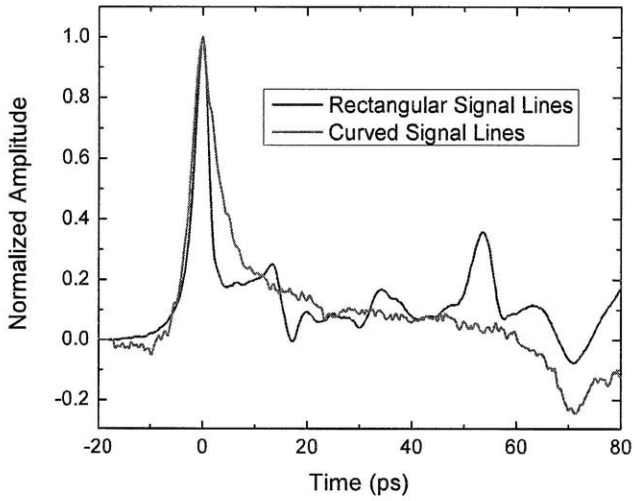

Figure 3-5: Characterization of coplanar waveguide topologies. In time, the first peak represents the detection of the voltage pulse that has traveled from the launch point, L, and reached the detection point, D. Other, lower amplitude peaks, are unwanted reflections due to the initial voltage pulse. The effective pulse width taken at ≈ 0.7 FWHM for an assumed Gaussian voltage pulse convolved with the Gaussian optical pulse was measured approximately as 2 ps.

[3]The coarse scan of the curved signal line data (red), compared to the rectangular scan (blue) is simply due to the lock-in amplifier time constant being set at a higher value during the blue curve scan, resulting in a lower noise. The coarseness of the data is due to an equipment setting and is not an attribute of the CPW design.

3.3 Fiber Coupled Waveguides

To perform temperature-dependent spectroscopy using the CPW, one needs to both cool and heat the waveguide and test specimen. The most conventional means of accomplishing this task is to place the device into a variable-temperature cryostat. However, optically accessing the two Auston switches forming the pump (L) and probe (D) sites could be a formidable task. To circumvent this issue, an approach implementing a fiber-coupled waveguide was chosen. This method requires accommodating two optical fibers (i.e, pump and probe beams) and still allowing room for the test sample. These requirements result in fabricating a specialized package that allows optical access to the CPW, while providing a sample space for placing the test specimen.

3.3.1 Fabrication of Fiber-coupled CPWs

To facilitate the coupling of optical fibers to the CPW a specialized package was developed, which allowed optical fibers to be epoxied to the package while withstanding liquid nitrogen temperatures and below. This feature is important, because if the optical connection breaks during a cool-down, then the measurement cannot proceed. Furthermore, the specialized CPW-stack (as it was referred to colloquially in the laboratory), provided a protective surface for the soft Au metal waveguide and allowed materials to be tested by placing them directly onto the CPW without scratching or damaging the Au surface shown in Fig. 3-2. Coplanar waveguides were fabricated using the microfabrication process described in section 3.2.1. The evolution of the CPW stack is shown through both photographs and illustrations in Fig. 3-6.

Using a 400 μm thick Si wafer (100-orientation), coated with 100 nm thick low-stress LPCVD nitride on both of its surfaces, a support structure was formed by etching vias (54.7°) into the silicon using tetramethylammonium hydroxide (TMAH, 25%). These vias, approximately 250 μm at their smaller end, were made to accom-

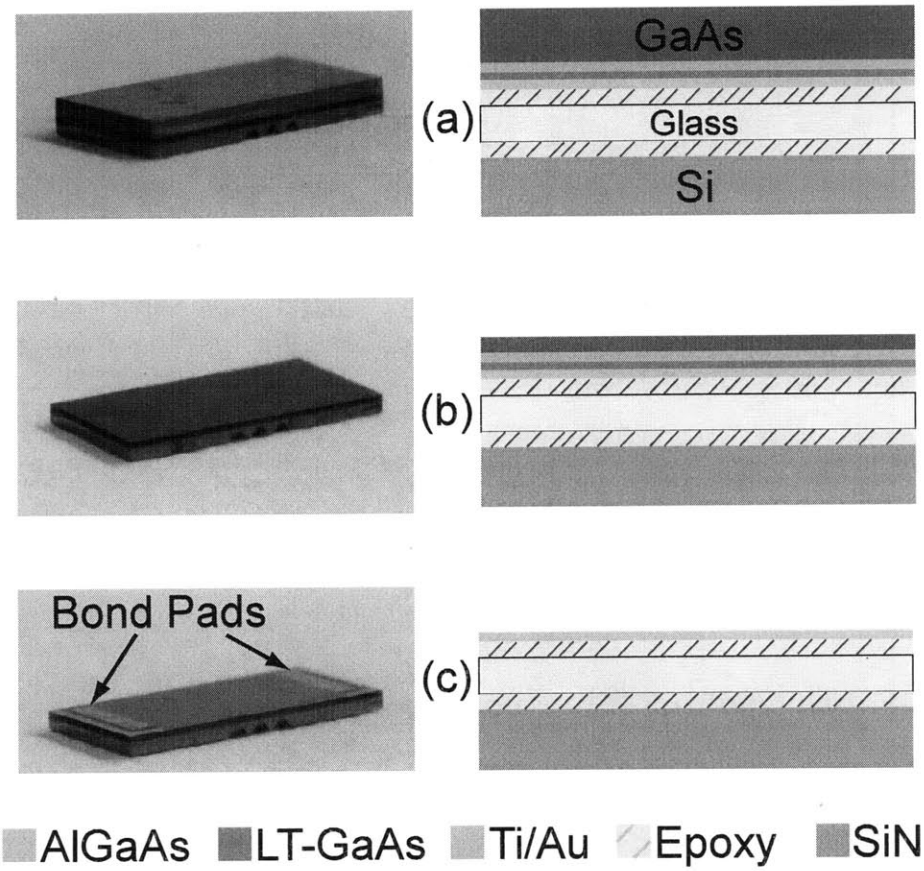

Figure 3-6: The encapsulated CPW package developed for optical fiber coupling to the pump and probe Auston switches. (a) A CPW was flip-chip bonded to a microscope cover slip (approximately 250 μm thick) with Gatan brand G1 epoxy. After curing, a Si substrate with TMAH etch vias was bonded to the aforementioned stack using G1 epoxy. During the epoxy-curing process, the pump and probe switches were aligned to the desired vias using an optical microscope. After all pieces were bonded, the stack was trimmed using a dicing saw. (b) The package was mechanically thinned using a polishing wheel, such that $\approx 50\,\mu$m of the original 650 μm substrate remained. To remove the remaining 50 μm, a citric acid-based etchant was implemented, with the etch terminating on the AlGaAs etch stop. (c) Using contact lithography, the ends of the chip where the contact pads reside were patterned and exposed (during photoresist development). Using the photoresist as an etch mask, the chip was dipped into a sulfuric acid-based etchant. This final step facilitated wire-bonding to the chip. *The illustrations show only the very end of the CPW-stack.*

modate an optical fiber (Thorlabs, 780 HP single mode) and allow it to be epoxied to the via sidewalls. Etching streets were patterned as well, such that once the via openings were completed individual pieces that were comparable in area to the CPW could be acquired. After the CPW was fabricated (as in section 3.2.1), it was flip-chip bonded to a microscope cover slip using Gatan brand G1 epoxy. After this assembly cured, it was mated to the Si via support substrate, as shown in Fig. 3-6 (a). During the epoxy curing process, the pump and probe Auston switches were aligned to two via openings using an optical microscope. After the entire stack was formed, the edges of the CPW-stack were trimmed using a dicing saw. To remove the GaAs substrate, the substrate was first thinned, using mechanical polishing, Fig. 3-6 (b). This process reduced the substrate thickness from 650 μm to $\approx$ 50 μm, which was necessary due to the relatively slow etch rate of GaAs in citric acid and peroxide (4:1, 0.25 μm/min.) at room temperature. The thinned chip was potted in crystal bond for protection with its top surface exposed and placed in a citric acid/hydrogen peroxide (4:1) bath [4] for approximately 8 hours, at which time the etch terminated on the $Al_{0.55}GaAs_{0.45}$ etch-stop layer. The LT-GaAs/AlGaAs layer that remains after this portion of the processing serves as a protective layer between the waveguide and the test specimen and has a total thickness of 1 μm. Because the conductor-ground plane spacing of the conductor was 10 μm, which is an order of magnitude less than the CPW-specimen spacing imposed by the LT-GaAs/AlGaAs protective layer, a substantial portion of field lines should remain transverse to the test specimen. [5]

Using the same contact lithography procedure for making the CPW itself, the top surface of the CPW-stack was coated with photoresist, with the far ends of the stack stripped of resist by light exposure and development. Using the resist as an etch mask, a sulfuric acid/hydrogen peroxide/DI water dip (1:8:80) was performed until the AlGaAs and LT-GaAs layers were completed etched at the chip's two ends and

[4]The citric acid was formed from citric acid powder and diluted 4:1 in deionized water.

[5]This order-of-magnitude estimate will be validated in future efforts, when finite-element simulations of various waveguide designs will be implemented.

the Ti/Au metal exposed, Fig. 3-6 (c). The completed chip was then epoxied to a 16 pin DIP (dual inline package) header.

3.3.2 Fiber-coupling to CPWs

A key requirement for the fiber-coupled Auston switches to work properly is that the optical fiber be placed such that the operation of the switch is maximized, i.e., the laser beam spot is at the center of the switch. Furthermore, if the optical fiber is to remain at the switch center by means of an epoxy, the fiber must remain at the switch center during the epoxy curing process. To address these issues, a fiber mounting and bonding station was assembled and is shown with detail in Appendix D. The heart of the system is given in Fig. 3-7 (a). This figure shows the CPW-stack mounted to a 16-pin DIP header (flipped upside down in the figure) and braced to an opto-mechanical post. The optical fiber is attached to an air chuck that can be positioned with high-resolution motion controllers. Using a distributed feedback (DFB) laser diode (780 nm) as a lighting source, the fiber was positioned to the center of the switch using a CCD camera placed on the opposite side of the CPW-stack. Figures 3-7 (b) and (c) show the laser without and with illumination when located at the switch center. After the alignment process, G1 epoxy was placed into the via using a wooden stick. The epoxy then wets the via and surrounds the fiber. To promote the curing process, a heat lamp was placed in close proximity to the CPW assembly.

An illustration showing the fiber inserted into the via is given in Fig. 3-8. From this illustration one will note how the laser light activates the switch by transmitting through the glass and epoxy [6]

The robustness of a fiber-coupled assembly was tested by dunking the fiber-coupled structure into a dewar of liquid nitrogen. Without fiber-coupling using the via in the CPW stack, i.e., mounting and epoxying a fiber to the top surface of the standard

[6]Based on an optical inspection of the completed part, the thickness of the epoxy appears to be only a few microns thick.

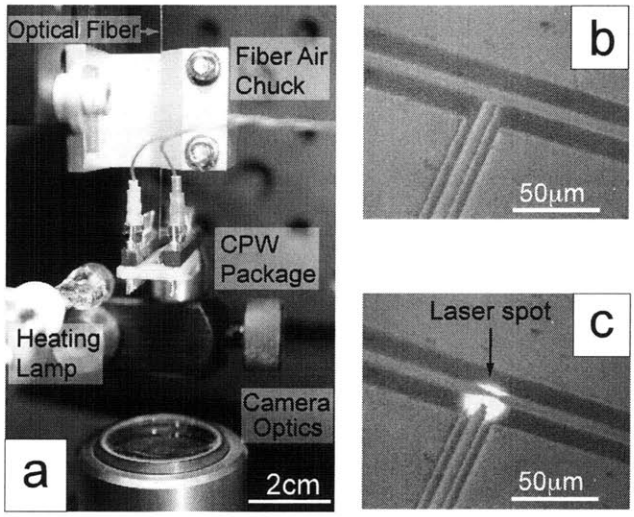

Figure 3-7: Fiber mounting and bonding to the CPW-stack. (a) The heart of the fiber bonding system, showing the CPW-stack package, the optical fiber clamped to the air chuck, heating lamp, and CCD camera optics for visual observation of the fiber location. (b) The switch as seen with the CCD camera. (c) The switch viewed with the CCD camera and illumination from the DFB laser.

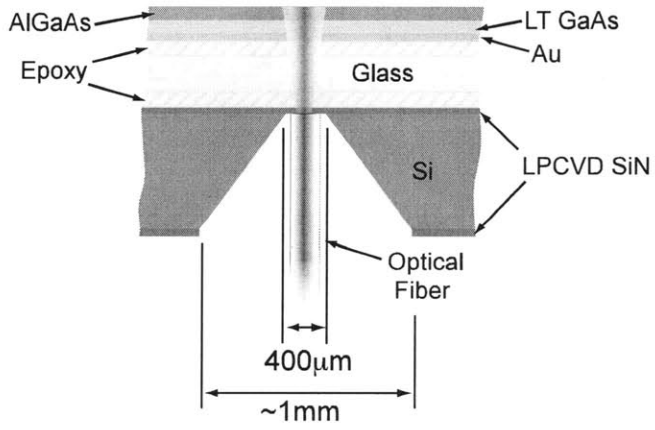

Figure 3-8: An illustration of the CPW (not to scale) showing an optical fiber routing through an etched opening in the silicon substrate. The optical fiber, with the cladding removed, is approximately 125 μm in diameter. This figure represents the cross-section of the device at either the launch (pump) or the detection (probe) location. The thicknesses of the Si and dielectric layers are given in sections 3.2.1 and 3.3.1.

CPW's Au surface, the assembly would fracture and become unusable. The experimental observation of the CPW-stack's via-coupled design surviving the liquid nitrogen dunk test resulted in its use in the final spectrometer design.

3.3.3 Fiber Optics Setup and Dispersion Compensation

To optically excite the fiber-coupled CPW stack, an optical-fiber-based experimental arrangement was assembled. This optical system is shown by a schematic illustration in Fig. 3-9. Using a fiber launcher, light is coupled into the optical fiber and divided using a 3 dB splitter, which is used to divide the initial beam into pump and probe beams. The pump beam is routed through an optical delay line and a 2-slot chopper wheel (coupled to lock-in amplifier to reduce system noise).

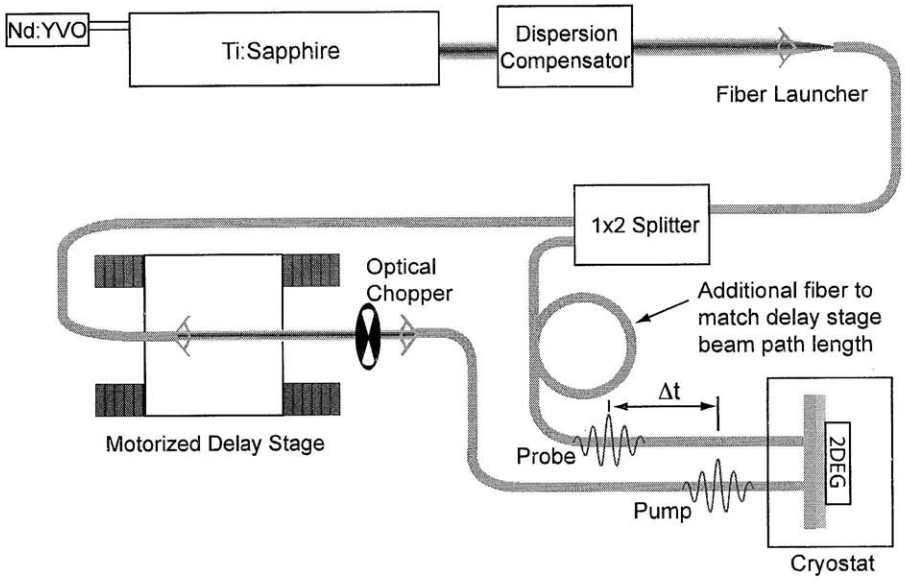

Figure 3-9: Optical system layout for fiber coupling to the cryostat enclosed CPW/2DEG stack.

Because the fused silica optical fibers exhibit negative dispersion [28], the longer

wavelength frequencies that comprise the 120 fs optical pulse from the mode-locked laser travel faster in the optical fiber than the shorter wavelength components. This physical phenomenon has a dramatic effect on the initial optical pulse, in that it causes the initial pulse to spread temporally by substantial amount. To overcome this matter, the optical pulse from the laser is "stretched" such that the long wavelength components are retarded in time before entering the fiber. This mechanism is often referred to as a pulse compressor or dispersion compensator. With a prescribed amount of optical fiber, one can stretch the pulse accordingly such that the initial pulse entering the fixed length of fiber is recovered. A schematic illustration for the dispersion compensator used in this work is given in Fig. 3-10, and a photograph of the mechanism with labeled components is given in Appendix B. The dispersion compensator consists of two diffraction gratings (1200 grooves/mm with a 750 nm blaze) and a front surface mirror.

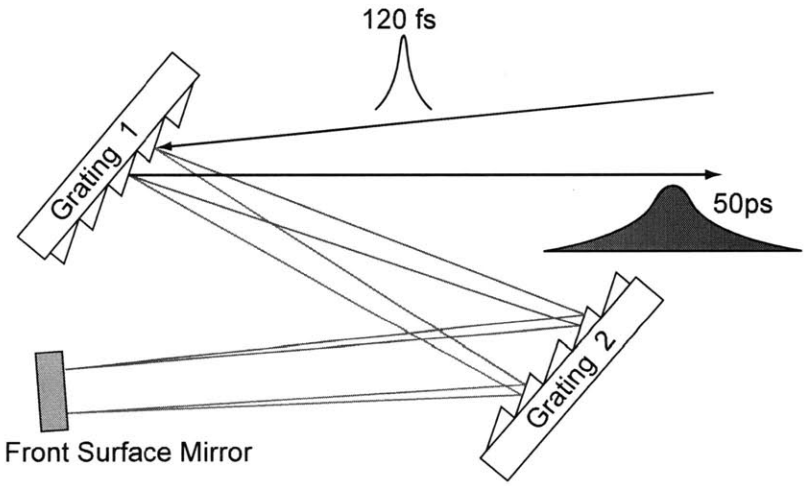

Figure 3-10: A dispersion compensator comprised of two diffraction gratings and a front surface mirror. The pulse entering the apparatus is 120 fs and the pulse exiting the system is approximately 50 ps.

The first grating in the system diffracts the light in the pulse into its constituent components, i.e., the colors are spread spatially and the second grating re-collimates

the beam. However, at the point the to beams are spread-out in space. Using a front surface mirror, the light is sent through both grating for a second pass, where the quantity of dispersion is doubled and the spatial wavelength distribution removed. To measure the effects of dispersion compensation, a fiber-coupled CPW-stack was used to time resolve a voltage pulse from the launch and detection sites along the waveguide. With the dispersion compensator absent, the measured pulse was approximately 50 ps. Figure 3-11 shows the change in the time-resolved voltage pulse for minor adjustments of the pulse compressor path length around the minimum attainable value of 3 ps. Away from the optimal path length, the pulse increases in time by either lessening the path length or extending the path length.

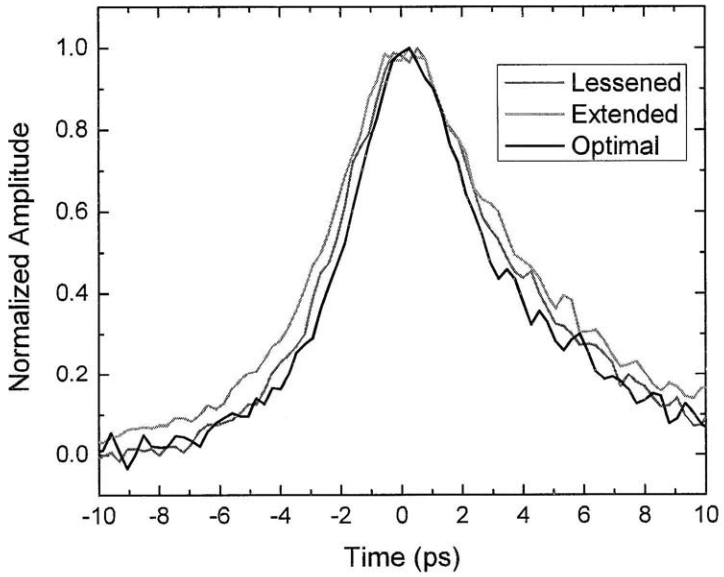

Figure 3-11: Optimization of the dispersion compensator path length. The minimum pulse achievable was 3 ps. The changes in the path length correspond to 1 mm changes in a total path length of 60 mm.

With an operational fiber-coupled CPW, the device was examined by testing its response for various values of incident optical power and pump (launch) switch voltage biasing. Figure 3-12 is a plot of the time resolved voltage pulse on the CPW-stack for

various optical powers and a pump (launch) switch voltage of 5 V. As expected, when the incident optical power to the switch is reduced, the magnitude of the voltage pulse reduces as well. The reduction in optical power corresponds to a reduction in free carriers generated in the Auston switch, which results in a lower photocurrent and measured voltage. An important and noteworthy item is that the first pulse reflection has changed locations temporally. The first unwanted pulse reflection is at 30 ps, for the CPW-stack rather than at 70 ps for the simple CPW on substrate device (confer with Fig. 3-5). This effect is due to the dielectric constant of the glass ($\varepsilon_{\text{glass}} \approx 4$), which is the majority of the substrate for the CPW, being much smaller than the dielectric constant of GaAs ($\varepsilon_{\text{GaAs}} \approx 13$), which is the substrate material used in the CPW free-space device. Recalling from Eqn. 3.2 (v_{ph}) and Eqn. 3.4 (ε_{eff}), and taking the dielectric constant of air to be approximately 1, one can obtain the following relationship

$$\frac{v_{ph,\text{glass}}}{v_{ph,\text{GaAs}}} = \sqrt{\frac{\varepsilon_{eff,,\text{GaAs}}}{\varepsilon_{eff,,\text{glass}}}} \approx \sqrt{\frac{7}{2.5}} \approx 1.7 \tag{3.7}$$

This estimate, which relies on the absence of modal dispersion along the CPW, shows that the phase velocity ($v_p h$), which can be approximated as the group velocity (v_g) for a nearly dispersionless system, for a wave in the CPW-stack is faster, compared to the case when a GaAs substrate is used. This effect can be circumvented and the reflection time increased by implementing sapphire ($\varepsilon \approx 11.5$) or GaP ($\varepsilon \approx 9$) rather than glass as the intermediate material in the CPW-stack.

Figure 3-13 shows the effects of varying the voltage on the pump (launch) switch and maintaining a constant incident optical power of 4 mW. The result of increasing the electric field across the Auston switch is a larger photocurrent, which increases the transient voltage pulse produced by the switch. As one increases the pump switch voltage the magnitude of the time-resolved voltage pulse increases, as shown in Figure 3-13. An interesting find (and one not shown in the data plots but observed in the laboratory) during this testing was witnessing a 1 V time-resolved voltage pulse

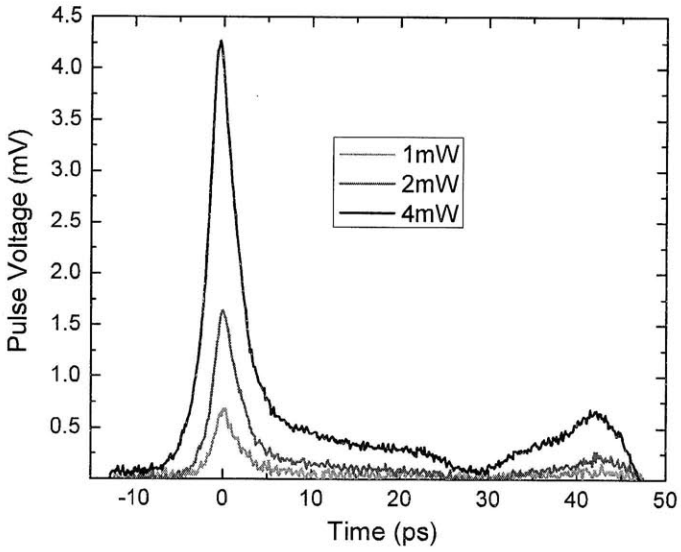

Figure 3-12: The measured effects of varying the incident optical power to the fiber-coupled CPW-stack. All scans exhibit the same magnitude reflections when normalized by the peak pulse. Although not shown in this plot, an optical power setting of 0.5 mW resulted in a peak voltage of 233 μV.

on the rectangular CPW (Fig. 3-4(a)), using a 100 V pump switch voltage. Such a high voltage was used on this guide because the author did not expect to use this device for any future testing. The ability to guide a 1 V picosecond voltage pulse could enable very interesting high-frequency gating measurements.

3.4 Waveguide Spectroscopy of the 2-D Electron Gas Plasmon

A collective oscillation of the conduction electron gas in a material is known as a plasma oscillation, and a quantum of this plasma oscillation is referred to as a plasmon [29]. In bulk materials, Drude theory reveals a plasmon resonance predominately at ultraviolet (UV) frequencies in metals, but in semiconductors, this plasmon resonance can exist in a range extending from mid-infrared to far-infrared in the electro-

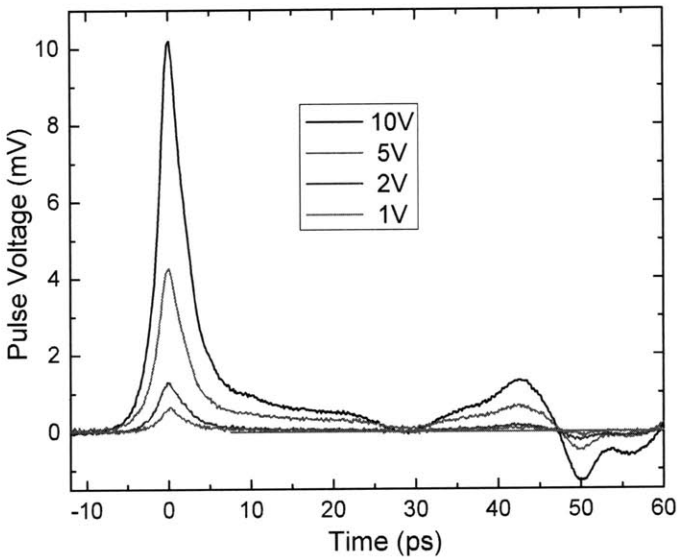

Figure 3-13: Time-resolved voltage pulses for a constant optical power of 4 mW and a variable pump switch voltage. All scans exhibit the same magnitude reflections when normalized by the peak pulse.

magnetic spectrum [30]. The plasmon frequency in both metals and semiconductors is proportional to the carrier density in the material [29]. In a metal the carrier density is essentially a constant, but in a semiconductor this carrier density can be altered.

A two-dimensional electron gas (2DEG), formed from a quantum well of GaAs, is essentially a sheet of charge that resides inside of the material. An important attribute of a quantum well 2DEG is that it possesses a tunable plasmon resonance, which can be altered by changing the 2DEG's carrier density (through electrical gating) or by setting the plasmon's wave vector, e.g., by implementing a grating [17]. The dispersion relation for 2D plasmon resonances in a heterostructure 2DEG is given by

$$\omega_p = \sqrt{\frac{e^2 n q}{2\,\varepsilon\varepsilon_o m^*}}, \tag{3.8}$$

where ω_p is the resonance frequency, e is the electron charge, $n = n(V_G)$ is the 2DEG carrier density at a gate bias V_G, q is the plasmon wave vector, $\varepsilon\varepsilon_o$ is the dielectric constant of the semiconductor, and m^* is the electron effective mass [30]. Another attractive feature of the GaAs 2DEG is that it can be fashioned with a relatively high mobility ($\mu \sim 10^6\,\mathrm{cm}^2/\mathrm{Vs}$ [31]), which for developing optical detectors from a 2DEG device allows for a high quality factor, Q, because of reduced damping.

3.4.1 Low-Temperature Measurement Setup

To perform low-temperature waveguide measurements on a 2DEG, an experimental setup was assembled, which consisted of a CTI Cryogenics closed system He cryostat, a Lakeshore 301 temperature controller, a Keithley 2400 source measurement unit for controlling the voltage on the pump switch, and a Signal Recovery 7265 lock-in amplifier for measuring the voltage at the detector switch, V_D. To facilitate measurements using the fiber-coupled CPW-stacks, optical fibers were routed into the cryostat using a compression fitting and a 1/8-inch tube potted with epoxy for sealing purposes. The cryostat with a fiber-coupled CPW-stack mounted onto the custom-machined copper sample holder is given in Fig. 3-14.

3.4.2 Expectations of Measurement Results

To better understand the behavior of a picosecond voltage pulse interacting with with a 2-D plasmon, a simulation was performed, where, using a Lorentz oscillator model for the effective dielectric constant of the 2-D plasmon, a picosecond voltage pulse was allowed to propagate along the waveguide and interact with the plasmon, with the resulting waveform examined to better understand how the 2D plasmon affects the initial voltage pulse. Considering a dielectric response with a resonance given as [26]

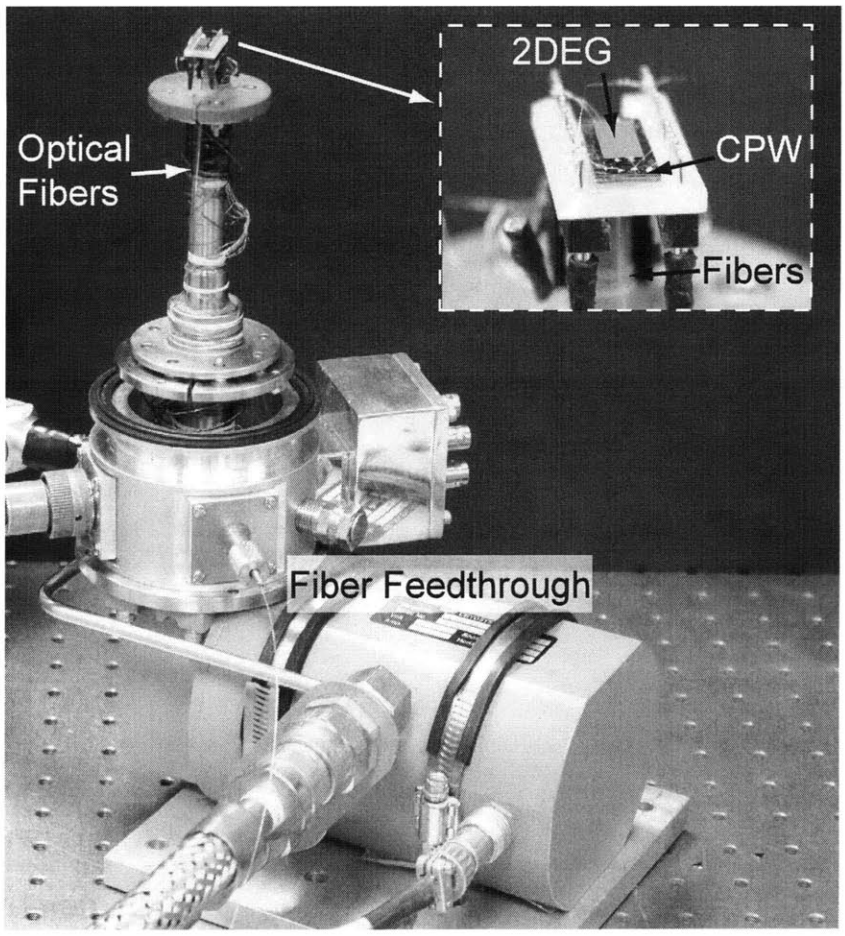

Figure 3-14: Optical system layout for fiber coupling to the cryostat enclosed CPW/2DEG stack. The inset shows the CPW-stack fiber-coupled and wire bonded to a 16-pin DIP header, with a 2DEG mounted on its top surface.

$$\varepsilon_r(f) = \varepsilon_\infty + \frac{f_p^2\,(\varepsilon_s - \varepsilon_\infty)}{f_p^2 - f^2 + i\gamma f}\,, \tag{3.9}$$

where f_p is the resonance frequency, ε_∞ is the high-frequency dielectric constant, ε_s is the low-frequency dielectric constant, and γ is a damping coefficient. To understand the propagation of a picosecond pulse along the guide, the voltage pulse was modeled as a gaussian pulse, $V(z,t)$, where z is the propagation direction and t is time. The pulse was first Fourier transformed from the time domain into the frequency domain

at $z = 0$, and then each frequency component of the pulse has its phase and magnitude modified by Eqn. 3.9 for a desired propagation distance. This result is then Fourier transformed into the time domain and produces a propagated voltage signal. This process is given mathematically as

$$V(z,t) = \mathscr{F}^{-1}\{\mathscr{F}\{V(0,t)\}e^{i\zeta(\omega)z}\}, \tag{3.10}$$

where $\mathscr{F}$ and $\mathscr{F}^{-1}$ are the Fourier transform and inverse Fourier transform, respectively, and

$$\zeta(\omega) = i\alpha(\omega) + \beta(\omega) = \frac{\omega}{c}\sqrt{\varepsilon_r(\omega)}. \tag{3.11}$$

The terms $\alpha(\omega)$ and $\beta(\omega)$ are the frequency attenuation and phase factors, respectively [32].

Simulations were performed using a plasma resonance of $f_p = 60\,\text{GHz}$ and $\gamma = 1/\tau = 10\,\text{GHz}$, where $\tau = 10\,\text{ps}$ corresponds to the scattering time. Two initial voltage pulse widths where chosen, one with a 1 ps width and another with a 3 ps width. The results of the voltage pulse propagation for both the 1 ps and the 3 ps pulses are given in Fig. 3-15 (a).

Figure 3-15 demonstrates that the effect of removing spectral content from the initial pulse, due to wave propagation and interaction with a resonant material, is evidenced by a "ringing" occurring in the tail of the propagated pulse.

3.4.3 Low-Temperature 2DEG Measurements

Using the low-temperature measurement system shown in Fig. 3-14, waveguide spectroscopy was performed on a 2DEG. First, with the CPW stack mounted in to the cryostat, a pump-probe measurement was performed on the sample without the 2DEG mounted. The results from this scan of the "bare chip", taken at a temperature of 298 K, are given in Fig. 3-16. After a 2DEG was placed on top of the CPW-stack

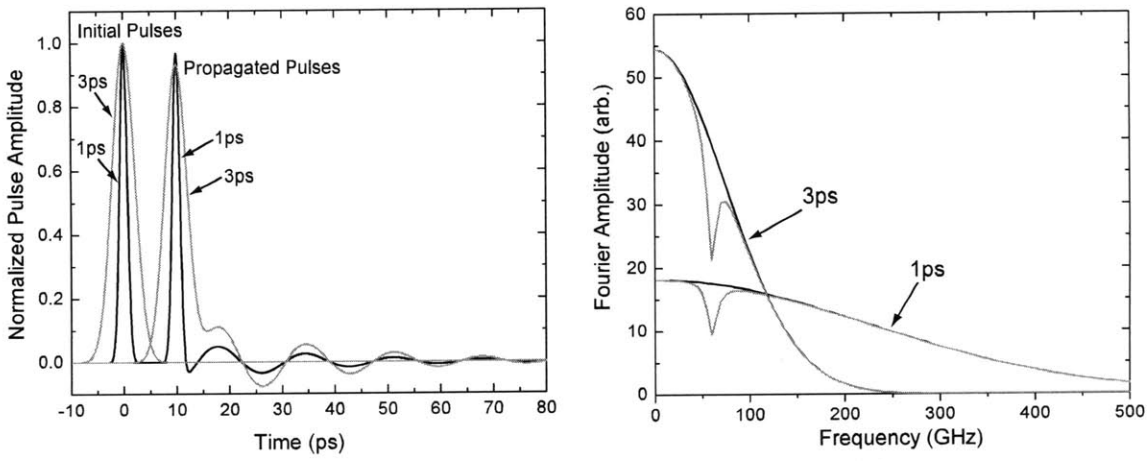

(a) (b)

Figure 3-15: Simulations of pulse propagation along the waveguide with the pulse interacting with a 2-D plasmon (a). Fourier transforms of both the initial and propagated pulses showing spectral content removed (with some bandwidth) at 60 GHz.

for testing, the measurement system was closed-up and evacuated to a pressure of $\sim 10^{-6}$ Torr. Remaining at 298 K a set of spectra was obtained with the 2DEG placed on top of the CPW-stack spectrometer. After this data was taken, the system was cooled to the cryostat's base temperature of 10 K, and a third and final scan was performed. The scans with the 2DEG placed on top of the CPW-stack at 298 K and at 10 K are given in Fig. 3-16.

Examining Fig. 3-16, one will note that the time-resolved voltage pulse has been altered by placing the 2DEG on top of the CPW, both at 298 K and at 10 K. A voltage reflection, observed in the range of -245 to -240 ps is most likely due to the sides of the 2DEG chip causing voltage reflections, as voltages travel out sideways along the curved pump and probe signal lines. This pulse reflection transpires more quickly in the 10 K sample, which is due to ε_{GaAs} possessing a lower value at 10 K compared to 298 K [33]. This effect is also the reason for the pulse height becoming larger in 10 K data. The expected "ringing" after the initial pulse, as shown by the simulation in Fig. 3-15 (a), is difficult to resolve due to the unwanted reflection in the 2DEG data

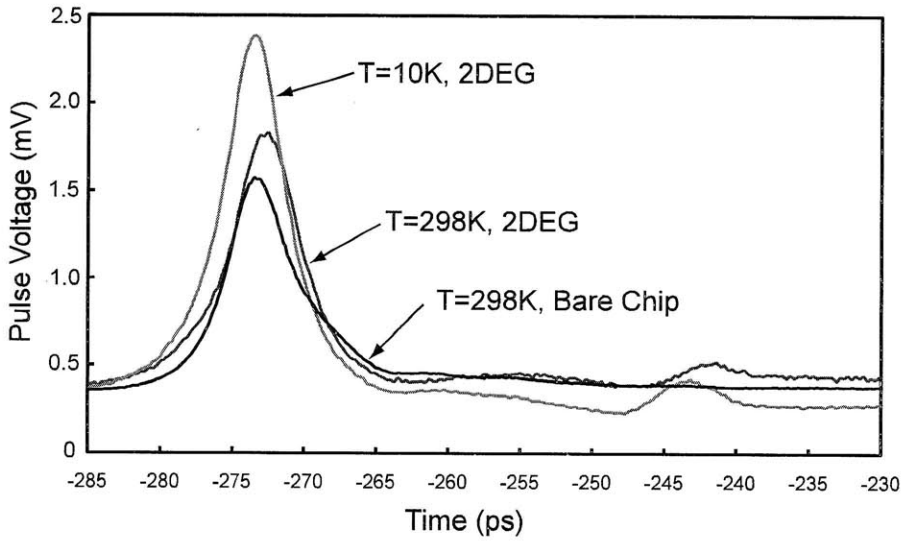

Figure 3-16: Time-resolved voltage pulses using the CPW-stack, with and without a 2DEG placed on its surface and at 298 K and 10 K. Due to the unwanted pulse reflections, the Fourier-transformed provided no usable information.

occurring near -243 ps. The 2DEG data does tend to show a slight amount of upward curvature after the initial pulse has been resolved, which is indicative of a plasmon resonance. However, because this effect was also observed in the 298 K 2DEG data, an unequivocal detection of the 2D plasmon cannot be determined without performing more measurements. Furthermore, when attempting to Fourier transform the time-resolved, propagated pulse, as done in Fig. 3-15 (b), the unwanted reflection resulted in cluttering the data such that an obvious absorption line could not be determined.

Using measured electronic properties of this exact 2DEG [31], a simulation was performed to determine what one may expect from this particular sample. Measured values for mobility, $\mu \approx 10^6\,\mathrm{cm}^2/\mathrm{V\text{-}s}$, and 2-D carrier density, $N_{2D} \approx 3 \times 10^{11}\,\mathrm{cm}^{-2}$, were used to estimate the scattering time, $\tau\,(= \mu m^*/e)$, and plasmon frequency, ω_p (as given by Eqn. 3.8). After computation, the values obtained were $\tau = 380\,ps$ and $\omega_p = 1.31 \times 10^{12}\,\mathrm{rad/s}$, which results in a predicted plasmon frequency of $f_p =$ 210 GHz. Due to the lower limit of temperature achieved in this measurement (10 K)

compared to the 0.3 K employed for the measured electronic property data, as an estimate, the scattering time was reduced to 30 ps for the simulation. The results of the simulation, implementing a 3 ps wide initial voltage pulse, are given in Fig. 3-17. The simulation data for the propagated voltage pulse shows evidence of the pulse tail being modified by interacting with the plasmon. However, the oscillations in the tail of this simulated pulse do not correspond well in time to the oscillations of the 10 K data shown in Fig. 3-16, as the first oscillation peak in the simulation occurs approximately 8 ps after the peak of the initial pulse, and in the measured data, this first oscillation peak in the pulse tail occurs at roughly 12 ps past the initial pulse peak.

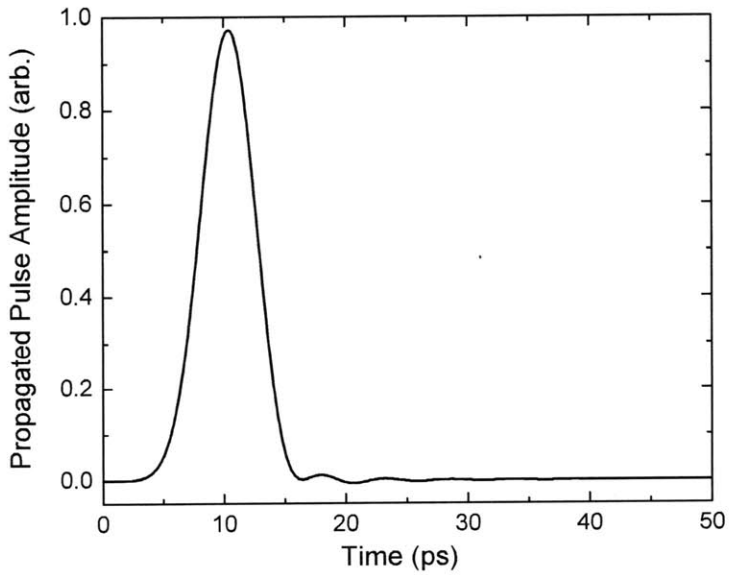

Figure 3-17: Simulated wave propagation of the 2DEG measured in Fig. 3-16, using measured electronic properties. Evidence of a plasmon oscillation is quite subtle.

3.5 Summary

This chapter described the development of a fiber-coupled CPW spectrometer that could be utilized at low-temperatures. The development of the spectrometer involved examining various CPW topologies such that Auston switches could be integrated into the device, without degrading the device performance by introducing unwanted voltage pulse reflections. Through pump-probe free-space measurements of two CPWs with differing topologies, a CPW signal and conductor line layout was determined that expanded the pulse reflection to approximately 70 ps, thus enhancing the capabilities of the CPW for use as a spectrometer. Such a large pulse reflection window on a CPW is not currently evident in the literature.

To enable fiber-coupled measurements, a fiber-coupling and bonding station was built such that fibers could be accurately attached to the pump and probe switches on the CPW. Also, an optical fiber optics setup was assembled, which included a pulse compressor to assist in reducing the effects of optical pulse dispersion from the laser.

A challenging and exotic microfabrication process was successfully attempted to form an encapsulated CPW that formed the CPW-stack used in fiber-based measurements in a cryostat. Such a device has not been demonstrated in the literature. Once fiber-coupled, this CPW-stack was examined by performing pump-probe measurements and varying both the optical excitation and pump switch voltage, to better understand the performance characteristics of the device. The CPW-stack withstood 10 K temperatures and remained optically and electronically functional during multiple cooling cycles.

To test the capabilities of the CPW-stack spectrometer a quantum well GaAs 2DEG was measured. The device showed a mild response to the presence of the 2DEG at both 298 K and 10 K temperatures. Voltage pulse propagation simulations were performed to gain insight into how a pulse propagating along the CPW would interact with a resonant dielectric material. Although similarities were observed between the

measured data and simulations, quite possibly the 3 ps spectrometer pulse may have lacked the necessary bandwidth to adequately interact with this material, as witnessed from plasmon resonance calculations of this 2DEG based on measured electronic property data taken at 300 mK.

Chapter 4

Conclusions and Future Work

4.1 Conclusions

The work presented in this thesis details the demonstration of a new type of encapsulated CPW spectrometer. A unique feature of this device is that the CPW is protected by an LT-GaAs/AlGaAs layer, which allows test materials to be placed in intimate contact with the device without damaging the waveguide. The CPW design topology implemented in the final device utilized a relatively large arc, rather than a right-angle bend, for the Auston switch pump and probe signal lines, to avoid unwanted reflections. This signal line topology permitted a large temporal window of 70 ps between the initial voltage pulse and the first unwanted reflection. Such large sampling-time windows for waveguide spectrometers do not exist in the current literature. A specialized, fiber-coupled CPW package, referred to as the CPW-stack in the previous chapter, permitted optical pump-probe measurements internal to a low-temperature cryostat. The CPW-stack remained fully functional at temperatures as low as 10 K, which was the base temperature of the cryostat.

The capabilities of this waveguide spectrometer were examined by using it to measure the plasmon resonance of a 2DEG. Although the CPW spectrometer showed a noticeable response when the 2DEG was placed in contact with the spectrometer,

resolving the plasmon resonance was inconclusive, most likely due to the limited bandwidth of the 3 ps spectrometer and the estimated 210 GHz plasmon resonance in the material tested.

4.2 Future Work

After completion of the measurements presented in section 3.4.3, many adjustments needed for improving the measurement became immediately apparent. The following section lists these topics and suggests how each could be addressed.

1. **Modeling and Measurement of Various CPW-stacks:** The CPW-stack design used in this work was chosen to minimize the distance between the test specimen and the CPW, while providing a protective surface for sample placement. Future work will involve measurements on a CPW-stack that is unprotected, i.e., the CPW is exposed on top of the LT-GaAs layer. An experimental comparison between the encapsulated CPW and the exposed CPW could provide insight into the effects of encapsulation. Furthermore, commensurate modeling and simulation of various waveguide assemblies using COMSOL software will be pursued to gain insight into the behavior of the CPW.

2. **Improve the 2DEG's contact to the CPW surface:** When placing the 2DEG sample directly on the CPW-stack, with only static friction (gravity) holding the sample in place, the sample can translate slightly around the surface of the CPW, potentially moving off of the CPW conductor line or impacting a wire bond and severing an electrical connection. This effect is believed to be a result of mechanical vibrations from the cryostat's cooling head. For the measurements performed in this work, small dollops of vacuum grease were employed to keep the 2DEG stationary. However, using vacuum grease may space the 2DEG slightly from the CPW and weaken electromagnetic coupling from the CPW to the 2DEG. A small mechanical clamp would be ideal, as it would

not prohibit coupling between the sample and the waveguide, as in the case of the grease. Attempts were made to use a spring-like structure for clamping in this work. However, the fragile nature of the CPW precluded achieving a robust mechanical spring attachment. A screw mechanism (consisting of many threads per turn) could potentially alleviate this problem.

3. **Increase the bondpad size and spacing:** Anticipating the use of Au wire bonding, the wire bond pads for the CPW-stack were fashioned to be approximately 200 μm x 500 μm. This geometry worked quite well for the standard CPW structures (Fig. 3-2). However, the flipped and encapsulated CPW-stack possessed exposed electrodes that are not Au, but, infact, the residue of the Ti/GaAs interface. This surface does not promote standard wire bonding. Furthermore, if a successful standard wire bond is made, this result may only be temporary, as these bonds may fail during the cryostat cool-down procedure. A work-around to this problem is to use a globule of indium for bonding. However, with inadequately sized bond pads, imprecise indium bonding can quickly result in electrical shorts between contact pads; a process that is essentially irreversible.

4. **Replace glass with sapphire:** Implementing glass as a support structure in the CPW-stack resulted in a wave propagation velocity along the guide that was faster than the standard CPW structure that uses GaAs as its dielectric support. The consequence of this action is that unwanted reflections from surfaces return faster and can obscure the data. Replacing the glass layer with sapphire would solve this problem, because the sapphire possesses a dielectric constant similar to GaAs and is optically transparent to the 780 nm light.

5. **Use a larger 2DEG sample:** Spurious reflections were caused by the 2DEG chip being too narrow, such that voltage pulses traveling along the pump and probe signal lines (and away from the pump and probe switches) were reflected

from the sides of the cleaved 2DEG. Although this material is expensive, a larger sized 2DEG piece that does not produce the aforementioned reflections should be re-useable.

6. **Vary carrier density with a back gate:** Implementing a back gate on the 2DEG would allow one to vary the carrier density in the structure, and adjusting this parameter would allow dynamic tuning of the 2DEG plasmon resonance. Furthermore, the unknown origins of the "bump" after the initial voltage pulse in Fig. 3-16, both at 298 K and 10 K, could have been more accurately determined by depleting the charge in the quantum well using a back gate.

7. **Experiment with multiple conductor-goundplane spacings:** As shown in Eqn. 3.9, the wave vector of the 2DEG directly controls its plasmon frequency. When measuring the 2DEG with a CPW, the conductor-groundplane spacing sets the wavelength and ultimately the wave vector of the plasmon. A transform-limited 3 ps ($= \Delta\tau$) pulse will contain approximately 50 GHz ($= \Delta f$) of bandwidth. In the measurements discussed in the previous chapter, the 10 μm conductor-groundplane spacing of the CPW, combined with the 2DEG's carrier density of 3×10^{11} cm^2, centers the plasmon resonance at 210 GHz. Increasing the conductor-groundplane spacing to 480 μm would center the plasmon frequency at 30 GHz, making plasmon detection more feasible.

8. **Improving the spectrometer's temporal resolution:** With optimal dispersion compensation and LT-GaAs annealing, optical-fiber-based waveguide measurements should possess a temporal resolution that is limited by the speed of an individual Auston switch on the waveguide. The characteristics of the Auston switch's speed, when integrated into a waveguide, are influenced by both the line impedance of the waveguide and capacitance of the switch gap. Improvements to the switch's speed, and thus the temporal resolution of the system, could be obtained by performing a pump-probe measurement on a sin-

gle Auston switch on the CPW and varying the line impedance and switch gap capacitance (through the use of multiple waveguides). Experimentally, one could determine a line impedance and gap capacitance that optimizes the speed of the switch.

Appendix A

Freespace Optics Arrangement

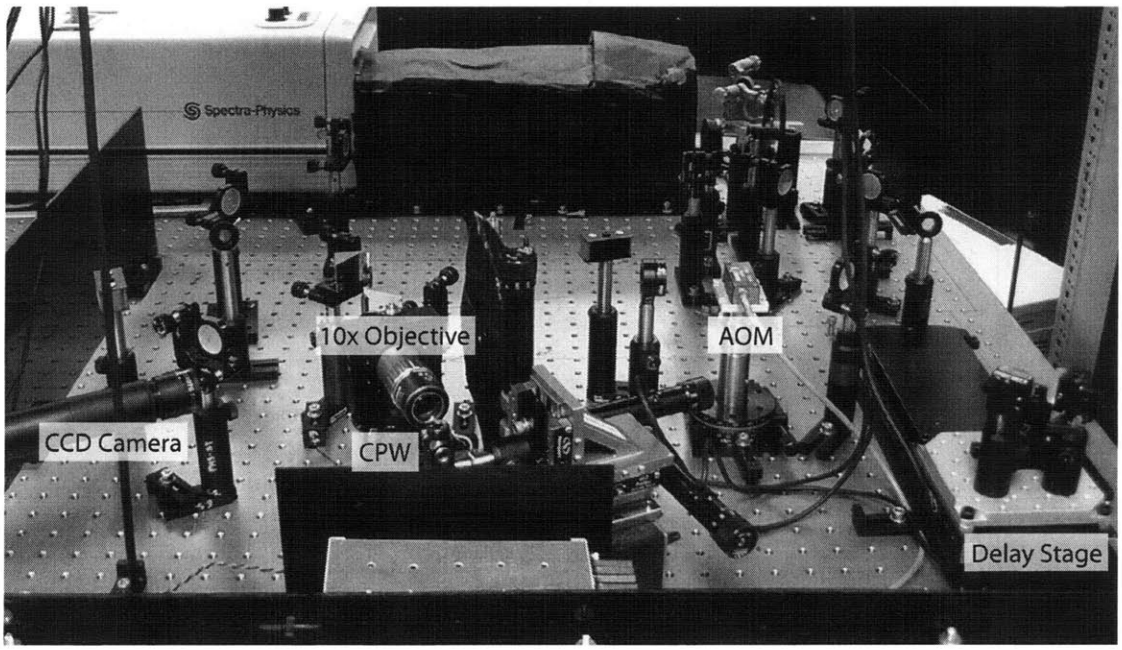

Figure A-1: Freespace optics setup for examining the carrier lifetime of LT-GaAs and the impulse response of the coplanar waveguides (CPWs) with integrated Auston switches. A few components of the arrangement are labeled to serve as a reference for the schematic given in Fig. A-2

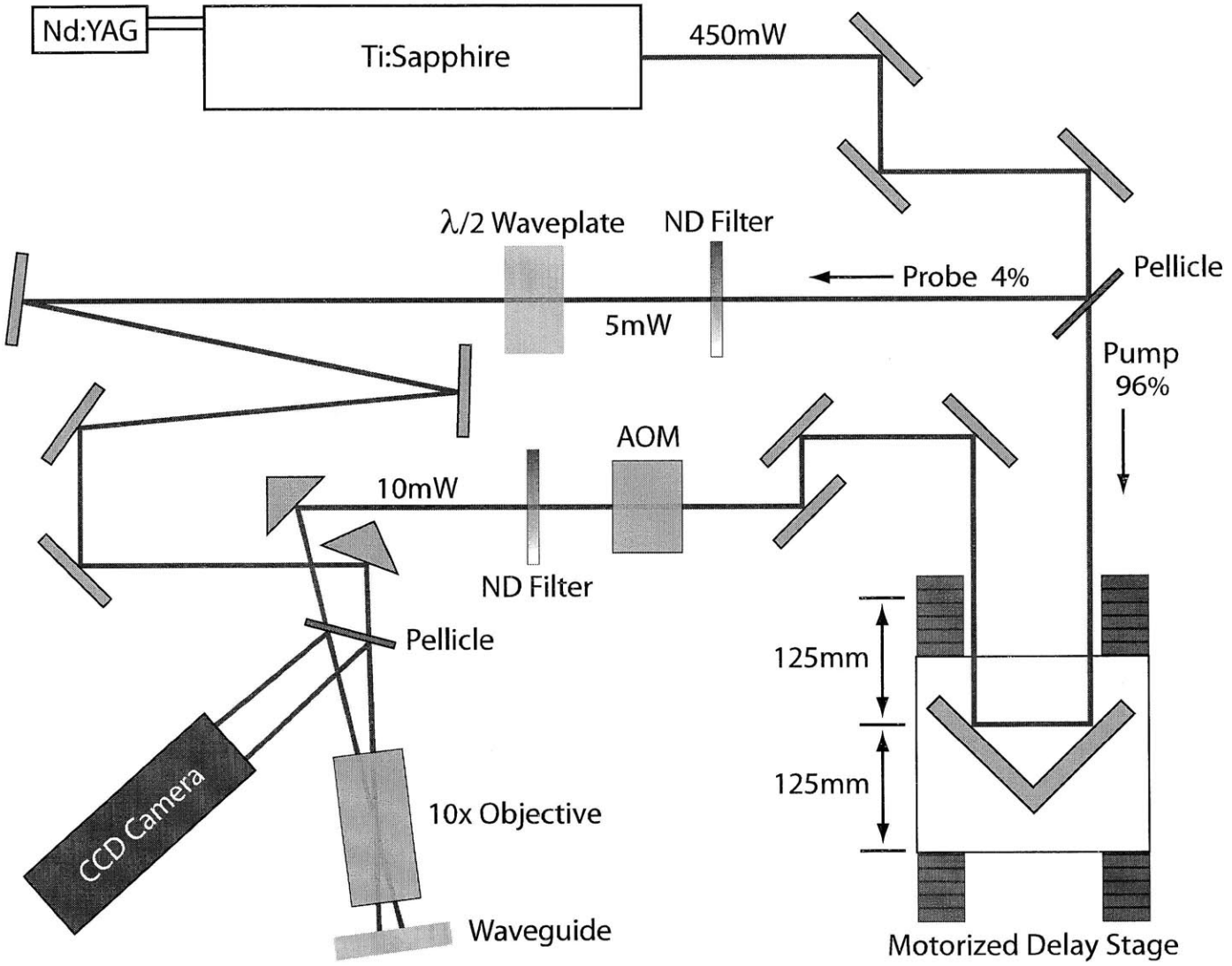

Figure A-2: Beam path and component diagram for the free-space carrier lifetime and CPW impulse response measurement. Undesired reflected and split beams, which are controlled with beam blockers, are omitted from the diagram for clarity.

Appendix B

Pulse Compressor Layout

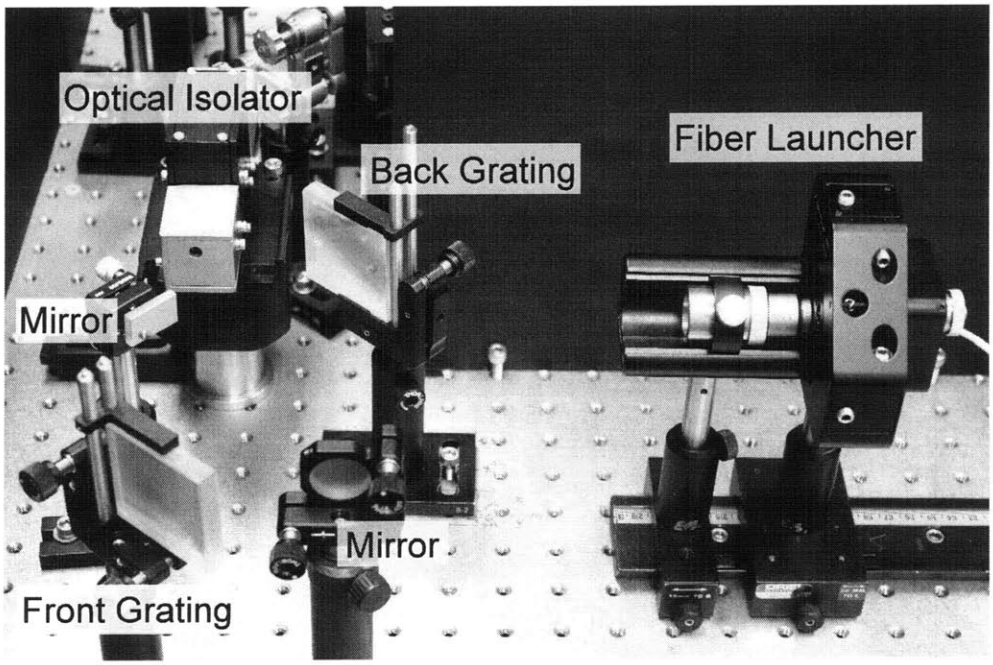

Figure B-1: The components of the dispersion compensator.

Appendix C

Fiber-Coupled Delay Stage

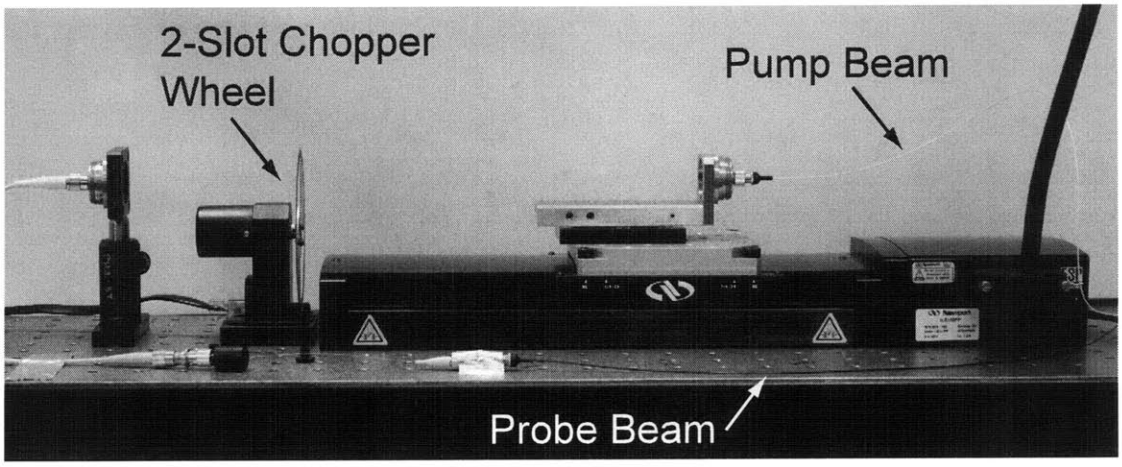

Figure C-1: A photograph of the fiber-coupled delay stage. A 3 dB optical fiber splitter is used to separate the pump and probe beams, with the pump beam sent through a delay stage and optical chopper.

Appendix D

Fiber Alignment and Bonding Setup

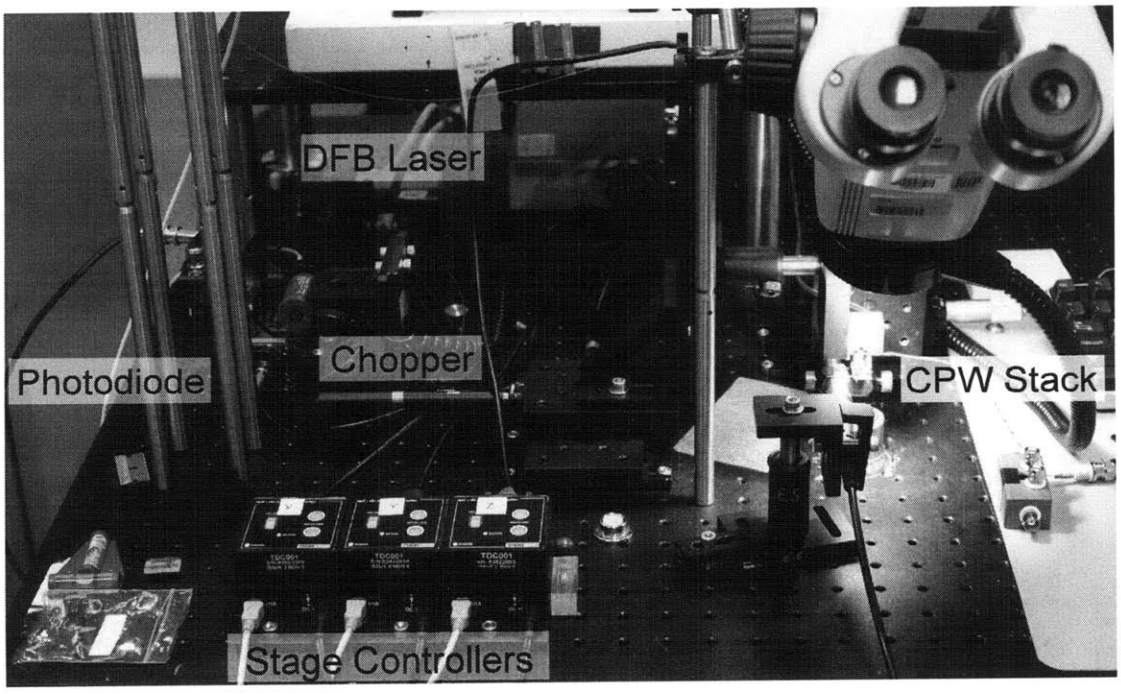

Figure D-1: A photograph of the fiber alignment and bonding setup.

Bibliography

[1] Gang Chen. *Nanoscale Energy Transport and Conversion.* Oxford University Press, 2005.

[2] A. Javey, J. Guo, Q. Wang, M. Lundstrom, and H. Dai. Ballistic carbon nanotube field-effect transistors. *Nature*, 424:654–657, 2003.

[3] D. C. Tsui, H. L. Stormer, and A. C. Gossard. Two-dimensional magnetotransport in the extreme quantum limit. *Physical Review Letters*, 48(22):1559–1562, 1982.

[4] R. Laughlin. Anomalous quantum hall effect. *Physical Review Letters*, 50(18):1395–1398, 1983.

[5] C. Toke, P. Lammert, V. Crespi, and J. Jain. Fractional quantum Hall effect in graphene. *Physical Review Letters*, 74:235417, 2006.

[6] Agilent network analyzers. www.agilent.com, September 2010.

[7] C. Karadi, S. Jauhar, L. P. Kouwenhoven, K. Wald, J. Orenstein, and P. L. Mceuen. Dynamic response of a quantum point contact. *J. Opt. Soc. Am.*, 11(12):2566, 1994.

[8] E. Chen and S. Chou. Group velocities in coplanar strip transmission lines on Si and Si/ Si O_2/ Si substrates measured using differential electro-optic sampling. *Appl. Phys. Lett*, 69(19):2861, 1996.

[9] Southeastern universities reasearch association, 2010.

[10] David M. Pozar. *Microwave Engineering.* Wiley, 3rd edition, 2004.

[11] E. A. Shaner. *Picosecond Waveguide Spectroscopy and Time-Resolved Ballistic Electron Transport.* PhD thesis, Princeton University, 2004.

[12] Clark Highstrete and Mark Lee. Disorder dominated microwave conductance spectra of doped silicon nanowire arrays. *Nano Letters*, 8(6):1557–1561, 2008.

[13] D. H. Auston. Impulse response of photoconductors in transmission lines. *IEEE J. Quantum Electron.*, 19:639, 1983.

[14] D. Grischkowsky, M. Ketchen, C. Chi, I. Duling, N. Halas, J. Halbout, and P. May. Capacitance free generation and detection of subpicosecond electrical pulses on coplanar transmission lines. *IEEE Journal of Quantum Electronics*, 24(2):221–225, 1988.

[15] Hecht. *Optics.* Addison Wesley, 2001.

[16] M. Golay. Theoretical consideration in heat and infra-red detection with particular reference to the pnuematic detector. *Review of Scientific Instruments*, 18(5):347–356, 1947.

[17] E. A. Shaner, M. C. Wanke, A. D. Grine, S. K. Lyo, and J. L. Reno. Enhanced responsivity in membrane isolated split-grating-gate plasmonic terahertz detectors. *Appl. Phys. Lett*, 90:181127, 2007.

[18] M. Y. Frankel, J. F. Whitaker, G. A. Mourou, F. W. Smith, and A. R. Calawa. High-voltage picosecond photoconductor switch based on low-temperature-grown gaas. *IEEE Trans. Electron Devices*, 37:2493, 1990.

[19] F. W. Smith. *The device applications and characterization of nonstoichiometric GaAs grown by molecular beam epitaxy.* PhD thesis, Massachusetts Institute of Technology, 1990.

[20] S. Gupta, M. Y. Frankel, J. A. Valdmanis, and J. F. Whitaker. Subpicosecond carrier lifetime in gaas grown by molecular beam epitaxy at low temperatures. *Appl. Phys. Lett*, 59(25):3276 – 3278, 1991.

[21] E. S. Harmon, M. R. Melloch, J. M. Woodall, D. D. Nolte, N. Otsuka, and C. L. Chang. Carrier lifetime versus anneal in low temperature growth gaas. *Appl. Phys. Lett*, 63(16):2248 – 2250, 1993.

[22] K. A. McIntosh, K. B. Nichols, S. Verghese, and E. R. Brown. Investigation of ultrashort photocarrier relaxation times in low-temperature-grown gaas. *Appl. Phys. Lett*, 70:354, 1997.

[23] B. R. Bennet, R. A. Soref, and J. A. del Alamo. Carrier-induced change in refractive index of inp, gaas, and ingaasp. *IEEE Journal of Quantum Electronics*, 26:113, 1990.

[24] P. Arafin, T. L. Tansley, and E. M. Goldys. Electron transport in low temperature grown gaas. *Optoelectronic and Microelectronic Materials And Devices Proceedings*, 1996.

[25] E. Chen and S. Chou. Characteristics of coplanar transmission lines on multilayer substrates: Modeling and experiments. *IEEE Transactions on Microwave Theory and Techniques*, 45(6):939–945, 1997.

[26] G. Hasnain, K. W. Goossen, and W. H. Knox. Effect of optical phonons on femtosecond pulse propagation in coplanar strips. *Appl. Phys. Lett*, 56(6):515–517, 1990.

[27] U. D. Keil, D. R. Dykaar, A. F. J. Levi, R. F. Kopf, L. N. Pfeiffer, S. B. Darack, and K. W. West. High-speed coplanar transmission lines. *IEEE Journal of Quantum Electronics*, 28:2333, 1992.

[28] B. E. A. Saleh and M. C. Teich. *Fundamentals of Photonics.* John Wiley and Sons, 1991.

[29] Charles Kittel. *Solid State Physics.* John Wiley and Sons, 8th edition, 2004.

[30] John Davies. *The Physics of Low Dimensional Structures.* Cambridge University Press, 1997.

[31] Michael Lilly. Personal communication. Sandia National Laboratories.

[32] J. H. Son, H. H. Wang, J. F. Whitaker, and G. A. Mourou. Picosecond pulse propagation on coplanar striplines fabricated on lossy semiconductor substrates: modeling and experiments. *IEEE Transactions on Microwave Theory and Techniques*, 41:1574, 1993.

[33] J. S. Blakemore. Semiconducting and other major properties of gallium arsenide. *Journal of Applied Physics*, 53:123–181, 1982.